MOLECULAR CLOUDS IN THE CARINA ARM: LARGE-SCALE PROPERTIES OF MOLECULAR GAS AND COMPARISON WITH H I

D. A. GRABELSKY, R. S. COHEN, L. BRONFMAN,[1] AND P. THADDEUS
Columbia University and Goddard Institute for Space Studies

AND

J. MAY
Universidad de Chile
Received 1986 June 9; accepted 1986 September 22

ABSTRACT

We report results from the first large-scale survey in the CO ($J = 1 \to 0$) line of the Vela-Carina-Centaurus region of the southern Milky Way. The observations, made with the Columbia University 1.2 m millimeter-wave telescope at Cerro Tololo, were spaced every beamwidth ($0°.125$) in the range $270° \leq l \leq 300°$ and $-1° \leq b \leq 1°$, with latitude extensions to cover all Carina arm ($l > 280°$) emission beyond $|b| = 1°$. In a concurrent survey made with the same telescope, every half-degree in latitude and longitude was sampled in the range $270° \leq l \leq 300°$ and $-5° \leq b \leq 5°$ at a spatial resolution of $0°.5$. Both surveys had a spectral coverage of 333 km s^{-1} with a resolution of 1.3 km s^{-1}.

The Carina arm is the dominant feature in the data. Its abrupt tangent at $l \approx 280°$ and characteristic loop in the (l, v)-diagram are unmistakable evidence for CO spiral structure. When the emission is integrated over velocity and latitude, the height of the step seen in the tangent direction indicates that the arm-interarm contrast is at least 13:1. Spatial maps of the arm exhibit a projected narrowing in latitude of the CO layer with increasing kinematic distance, lending support to the kinematically implied picture of the arm. Comparison of the CO and H I data shows close agreement in a segment of the arm lying outside the solar circle ($R_0 = 10$ kpc); within R_0 the arm is more difficult to trace in H I than in CO.

The distribution of the molecular layer about the Galactic plane in the outer Galaxy is determined on the basis of the assumption of axial symmetry with respect to the Galactic center. Between $R = 10.5$ and 12.5 kpc, the average CO midplane dips from $z = -48$ to -167 pc below the $b = 0°$ plane, following a well-known similar warping of the H I layer. In the same range of radii, the half-thickness of the CO layer increases from 112 to 182 pc, mimicking the long-recognized flaring of the H I layer in the outer Galaxy.

Subject headings: galaxies: Milky Way — galaxies: structure — interstellar: molecules

I. INTRODUCTION

A spiral arm of the Milky Way in Carina was first proposed by Bok (1937), only 14 years after spiral nebulae were conclusively shown to be distant, extragalactic systems. This suggestion, based on Bok's observation of the distribution of distant, young stars in Carina, subsequently found confirming evidence in virtually every study of Population I along the Milky Way in Vela, Carina, and Centaurus. Sher (1965) pointed out that a pronounced transition at $l \approx 280°$ between the high concentration of bright Hα emission regions toward Carina ($l \geq 280°$) and the comparative absence of such regions preceding Carina in longitude, evident in the Hα atlas of Rodgers *et al.* (1960), corresponded to an abrupt intensity jump in the radio continuum maps of Mathewson, Healy, and Rome (1962), indicating that the optical edge is real and not merely due to foreground extinction. Sher argued further that the O and B stars, Cepheids, young clusters, and emission nebulae, distributed over considerable distances in a narrow longitude range about $l \approx 287°$, appeared to trace a spiral arm aligned nearly parallel to the line of sight in Carina and that the edge at $\sim 280°$ marked the tangent direction of the arm. Graham (1970) reached a similar conclusion from the objective prism survey of Graham and Lyngå (1965) of several hundred OB stars, finding

that the stars are spread out over distances from 2 to 10 kpc between 282° and 292° and that their distribution has a sharp outer boundary that becomes more distant with longitude. The H109α radio recombination line survey of Wilson *et al.* (1970) showed that H II regions similarly trace the Carina arm.

Bok, Hine, and Miller (1970), from a comparison of Population I studies in Carina, provided what has become the generally accepted picture of the Carina arm: the arm opens outward starting from a point ~ 2 kpc from the Sun near $l = 295°$; is viewed tangentially at $\sim 283°$, where it crosses the solar circle; then extends to ~ 10 kpc from the Sun as it curves gently toward higher longitude. A lane of neutral hydrogen emission beyond the solar circle, corresponding to the distant portion of the Carina arm, was observed in early 21 cm surveys of the southern Milky Way and more recently with the Parkes 18 m telescope (Henderson, Jackson, and Kerr 1982, hereafter HJK). Optical extinction in the Carina region being generally quite low (Bok, Hine, and Miller 1970; Sundman 1979; Loden and Sundman 1980; Neckel and Klare 1980), the Carina arm provides a rare example of a Galactic arm delineated over several kiloparsecs by standard radio and optical spiral tracers.

The recognition that nearby giant molecular clouds spawn massive O and B stars (e.g., Tucker, Kutner, and Thaddeus 1973; Kutner *et al.* 1977), which, with their bright optical H II regions, trace optical spiral structure locally in the Galaxy and in external galaxies, strongly implied that molecular clouds are

122

themselves fundamental components of large-scale spiral structure. Further, giant molecular clouds observed in CO are, like H I, detectable throughout the disk of the Galaxy, so they provide an observational link between local optical arms and the classic 21 cm arms. From a study of the largest molecular clouds in the first Galactic quadrant, Dame *et al.* (1986; see also Dame 1983) concluded that giant molecular clouds are indeed excellent tracers of spiral structure, exhibit higher arm-interarm contrast than H I, and generally appear to be closely associated with distant radio H II regions. Nevertheless, differences of opinion persist regarding the usefulness of CO as a spiral tracer and the degree to which molecular clouds are confined to the Galaxy's spiral arms (see, e.g., Liszt and Burton 1981; Solomon, Sanders, and Rivolo 1985; Cohen *et al.* 1980; Dame *et al.* 1986). The claim that molecular clouds constitute a high-contrast tracer of the Galaxy's spiral arms could be tested further by determination of the large-scale distribution of H_2 in a region where spiral structure can be traced optically over large distances. Such a region is found in the Vela-Carina-Centaurus section of the Milky Way.

The first systematic search for CO in the southern Galaxy was made in the $1 \to 0$ line by Gillispie *et al.* (1977). Five detections were made between $l = 284°$ and $300°$ in the directions of well-known H II regions, including the Carina nebula, NGC 3576, and NGC 3603. Subsequently, the Carina nebula was observed in the $2 \to 1$ transition and mapped over a small region by de Graauw *et al.* (1981). Further observations in the $2 \to 1$ line toward individual sources were made by White and Phillips (1983). In a more extensive $1 \to 0$ survey at $b = 0°$ made with the 4 m telescope at CSIRO (McCutcheon *et al.* 1983; Robinson *et al.* 1984), the distant portion of the Carina arm was barely detected, because this part of the arm lies almost entirely below the plane; the tangent region, in particular, lying outside the low-longitude boundary (294°) of the survey, was completely missed. A CO $2 \to 1$ survey by Israel *et al.* (1984) covered $l = 270°$ to $355°$ at $b = 0°$, but again, owing to sparse sampling, restricted latitude coverage, and low sensitivity, the Carina arm went largely undetected.

In 1983 the first well-sampled, large-scale CO $(1 \to 0)$ survey of molecular clouds in the Carina arm was carried out with the Columbia Millimeter-wave Telescope at Cerro Tololo, Chile. Preliminary results were reported by Cohen *et al.* (1985), who showed that the arm is traced exceptionally well over 25 kpc by molecular clouds and that it apparently joins the Sagittarius arm, defined by molecular clouds in the Columbia CO survey of the first quadrant (Dame *et al.* 1986). In this and a future paper we present the observations and analysis leading to the conclusions of Cohen *et al.* and amplify some of the early results.

The Carina arm is the dominant feature in our CO data, and the close agreement between the CO and the classic pictures of the arm emphasizes the importance of CO as a tracer of Galactic spiral structure. In this paper we concentrate on the large-scale properties of molecular gas in the Carina region: how it is distributed in space and radial velocity and its degree of concentration to the spiral arm. Comparison to the H I distribution demonstrates both the striking similarities in the H_2 and H I distributions—supplying strong evidence for the connection between CO and H I spiral structure—and the relative advantages of CO as a Galactic spiral tracer. The physical association of the bright optical and radio tracers of the Carina arm with the individual molecular clouds observed in our survey, and the long-standing question of how the Carina arm

connects with other spiral arms in the Galaxy, will be treated in a forthcoming paper (see also Grabelsky 1985); some specific Carina arm molecular clouds and related star-forming regions are mentioned here as needed, but the reader should refer to Grabelsky (1985) for details. In our comparison to H I here we touch on the problem of the Carina arm in the Galaxy. The observations are presented in the next section (II); in § III we discuss the results, including the H I comparison. We summarize the results in § IV.

We completed our analyses just prior to the recent recommendation by IAU Commission 33 for adoption of revised values of the galactocentric distance of the Sun R_0 and the galactocentric circular velocity of the local standard of rest V_0 (see Kerr and Lynden-Bell 1986). Throughout this paper we use the *old* values, $R_0 = 10$ kpc and $V_0 = 250$ km s^{-1}, primarily to facilitate comparison of our results with most previous Galactic CO and H I studies, which were based on the old values. The qualitative conclusions reached here are not altered by the changes in the values of R_0 and V_0. The quantitative effects of these revisions ($R_0 = 8.5$ kpc and $V_0 = 220$ km s^{-1}) on our results are discussed in the Appendix.

II. OBSERVATIONS

a) Instrumentation

The observations were made between 1983 January and November with the Columbia Southern Millimeter-wave Telescope at Cerro Tololo, or Chile Telescope for short, a close copy of the Columbia Northern Millimeter-wave Telescope, or New York Telescope. The antenna of the Chile Telescope is a fast Cassegrain reflector with a 1.2 m parabolic primary and a 18.8 cm hyperbolic secondary. The primary has a maximum surface inaccuracy of ~ 12 μm ($\lambda/200$ at 2.6 mm), including gravitational deformation. With a 115 GHz transmitter on Cerro Morado, a mountain ~ 4 km from Cerro Tololo, the antenna pattern was measured and shown to be in close agreement with that calculated from diffraction theory (Bronfman 1986); the full width of the main beam at half-intensity was measured to be 8'.8. Signal detection is accomplished with a double-sideband receiver incorporating a very stable liquid nitrogen cooled (77 K) Schottky barrier diode mixer; the receiver is followed by a filter bank spectrometer with 256 channels, each 0.5 MHz wide. The receiver had a single-sideband noise temperature of typically ~ 380 K measured at the scalar feed horn (Bronfman 1986). At 2.6 mm, the spectrometer has a velocity resolution (i.e., channel width) of 1.3 km s^{-1} and a total bandwidth of 333 km s^{-1}. A slight excess positive noise level (~ 1 σ at the sensitivity of this survey) in three channels, noticeable only when spectra are summed together channel by channel, was eliminated during data reduction by using a simple interpolation procedure (Grabelsky 1985). The telescope's altitude-azimuth mount is made to point and track under the control of a Data General Nova 4/X minicomputer, which also handles data acquisition and enables the observer to process spectra data while observing. Pointing was initially determined and subsequently checked (typically every 3-4 months) with a small optical telescope mounted on the primary and coaligned with the radio axis (the pointing model was the same one used for the New York Telescope; for details see Cohen 1977). The measured positions of ~ 40 stars showed the telescope pointing to be accurate to better than 1', or $\sim 1/10$ of the beam (Grabelsky 1985). Additional, daily pointing checks were made against the radio center of the Sun.

b) Calibration and Observing Method

All line intensities given here are antenna temperatures corrected for atmospheric attenuation and main beam efficiency and are equal to the radiation temperature T_R for a source that just fills the main beam. The receiver was calibrated using the standard chopper-wheel technique with modifications described by Kutner (1978). The resultant antenna temperatures, corrected for atmospheric losses, were scaled to agree with the calibration of the New York Telescope (Cohen, Dame, and Thaddeus 1986), using a number of standard sources. The difference between the two temperature scales is due primarily to the slightly different beam efficiencies and to an uncertainty in the oxygen opacities used in correcting for atmospheric losses. The relative calibration is estimated to be accurate to 5%, the sources of error being uncertainties in coupling efficiencies for the calibration sources and, again, in the oxygen opacities (Bronfman *et al.* 1986). A more accurate absolute and relative calibration of the New York and Chile Telescopes is currently being carried out, and the line temperatures presented here may be subject to corrections of 5%–10%.

Observations were made by position switching against reference positions verified to be free of CO emission. Elevation differences between source and reference positions were generally kept to less than $\frac{1}{2}°$. Integration times were typically 5 minutes, yielding an rms noise per channel of ~ 0.14 K. Straight lines were subtracted from each spectrum to determine the baseline; spectra which then showed baseline curvature greater than twice the rms were rejected and the positions reobserved. Typical spectra from the survey are shown in Figure 1.

c) The Surveys: Coverage and Data Presentation

Our basic strategy was to observe at low angular resolution the entire region in and around the Carina arm to fairly high latitude and in an independent survey to observe at high resolution the dense, distant material near the plane. Both extended from $l = 270°$ to $300°$ and covered 333 km s^{-1} (centered at $v_{LSR} = 0$) with a spectral resolution of 1.3 km s^{-1}, but differed in latitude coverage and spatial resolution. The main or full-resolution survey covered $|b| \leq 1°$, with some latitude extensions at $l > 280°$ (the tangent direction of the Carina arm) to cover all Carina arm sources. The spatial resolution was 8′8 (one beam), and the sampling was every 0°125 in l and b. This survey contains ~ 5500 spectra and covers about 85 deg^2.

The companion low-resolution survey covered $|b| \leq 5°$ at a spatial resolution of 0°5 with a sampling interval of 0°5 in l and b. By computer-controlled stepping of the telescope's position through a 4 × 4 raster during data acquisition, and summation of the resultant spectra, the half-degree resolution is implemented entirely in software. The low-resolution survey was carried out for three reasons: (1) to provide a quick overview of the CO emission in the Vela-Carina-Centaurus region of the Galactic plane; (2) to help determine appropriate latitude limits for the full-resolution survey; and (3) to map local, wide-latitude molecular clouds in the foreground. The low-resolution survey consists of 1281 spectra covering 300 deg^2.

Where the Carina arm extends beyond $l = 300°$, observations from a third, adjoining survey carried out concurrently on the same telescope (Bronfman 1986) are used in the analysis.

The velocity-integrated CO emission from the low-

resolution survey, integrated from -50 to $+50$ km s^{-1} for $|b| \leq 2.5$ and from -20 to $+20$ km s^{-1} for $|b| > 2°5$, is shown in the plane of the sky in Figure 2a. Containing no velocity information, this map, similar to that of radio continuum emission, is useful to show the apparent locations of
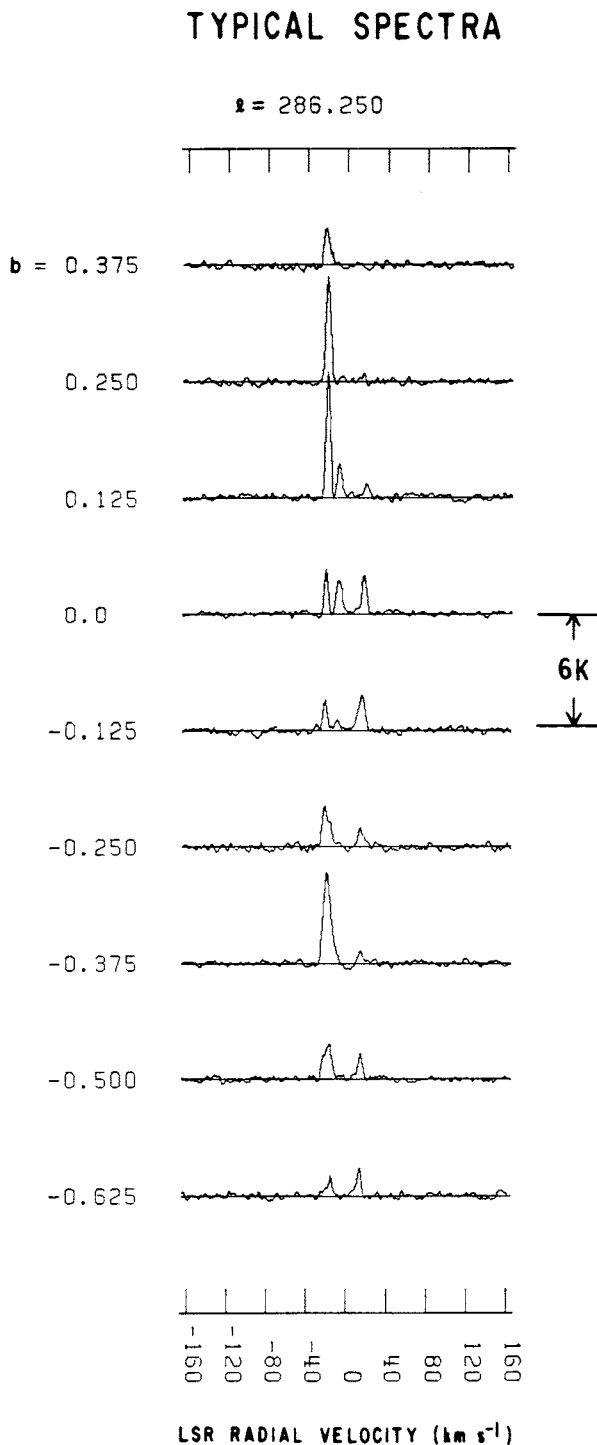

FIG. 1.—Sample spectra from the full-resolution survey. All spectra cover ~ 333 km s^{-1} with 256 channels, each 1.3 km s^{-1} wide. A linear baseline fit to the first and last 40 channels was removed from each spectrum. Typical integration times were 5 minutes, yielding a noise of ~ 0.14 K rms per channel. The intensity scale is in units of radiation temperature.

molecular clouds without regard to their distribution along the line of sight. For example, between $l = 270°$ and $280°$ the CO emission is diffuse and has a large latitude extent, while for longitudes above $280°$ it occurs largely in well-defined molecular clouds near the Galactic plane. The wide-latitude emission is mainly local, and the narrow layer is the much more distant Carina arm.

The similar spatial map in Figure 2b is a hybrid of the low-resolution map in Figure 2a and the data from the full-resolution survey integrated from -50 to $+50$ km s^{-1}. Figure 2b demonstrates that the latitude coverage of the full-resolution survey is sufficient to cover all the Carina arm clouds: outside the dotted line, where the low-resolution data are shown, wide-latitude emission at $l < 280°$ is seen, but little else. The figure also shows that the molecular clouds in the low-resolution map possess considerable unresolved structure; in particular, the region between $l = 280°$ and $285°$ is quite complex. From $285°$ to $295°$, strong sources immersed in the complex, low-level background appear clustered on scales of $\sim 1°$, suggesting that the smaller beam resolves big molecular clouds.

The largest molecular clouds stand out clearly when the chaff of small clouds is removed by "clipping": setting all spectral channels below about 3 σ (0.5 K) to zero before integration. Such maps (integrated from -100 to $+100$ km s^{-1}) are shown in Figures 3a (low-resolution) and 3b (the low- and full-resolution hybrid). Even with velocity blending, the main large clouds are readily distinguished in these maps. Most of

the emission between $l = 285°$ and $288°$, for example, is part of a large cloud complex associated with the η Carinae nebula. The emission between $289°$ and $290°5$ near the plane is a cloud associated with the H II region RCW 54a, and most of the emission between $291°$ and $296°$ comes from a cloud complex associated with the H II regions NGC 3576, RCW 60, RCW 61, and RCW 62.

The kinematics of molecular gas in the Galactic disk is best studied by displaying the data in the longitude-velocity plane, as in Figure 4. This (l, v)-map of most of the fourth quadrant was produced by integrating, *without clipping*, the full-resolution data over all latitudes where observations were made. Although the integration limits are not entirely uniform in l, they include essentially all nonlocal (Carina arm) emission at longitudes between $280°$ and $300°$, as indicated by the spatial map (Fig. 2). For $l > 300°$, only full-resolution data were available, but the Carina arm (seen in this part of the (l, v)-diagram as the lane of positive velocity emission) is covered completely within the latitude limits of the survey of this region of the fourth quadrant.

The dominant feature of the (l, v)-map is the open loop of emission at negative velocity from $l \approx 280°$ to $300°$ and positive velocity at $l \geq 280°$, joined by the intense emission centered at $v \approx 0$ km s^{-1} near $l = 280°$ (see schematic, Fig. 5). This loop is the Carina arm, its near side traced by the negative velocity emission, its far side by the positive velocity emission, and its tangent marked by the strong emission connecting the two. This map is discussed further in § III. (The strong,
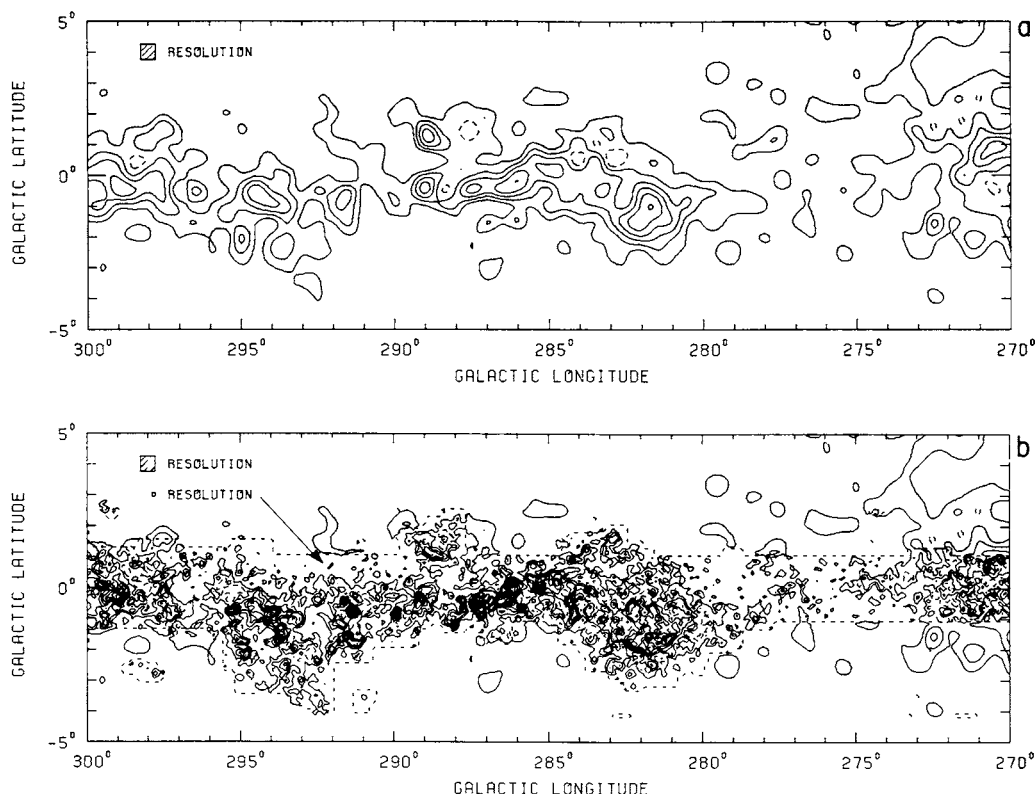

FIG. 2.—(a) Spatial map from the low-resolution survey showing all CO emission between $v = -50$ and $+50$ km s^{-1} for $|b| \leq 2.5°$; for $|b| > 2.5°$ the emission is integrated between $v = -20$ and $+20$ km s^{-1}. Contours are at integer multiples of 6 K km s^{-1}. (b) Spatial map combining both the low-resolution data, with velocity integration as described in (a), and the full-resolution data integrated between $v = -50$ and $+50$ km s^{-1}. The full-resolution data are shown within the dotted lines, the low-resolution data beyond. Contours are at integer multiples of 6 K km s^{-1}.
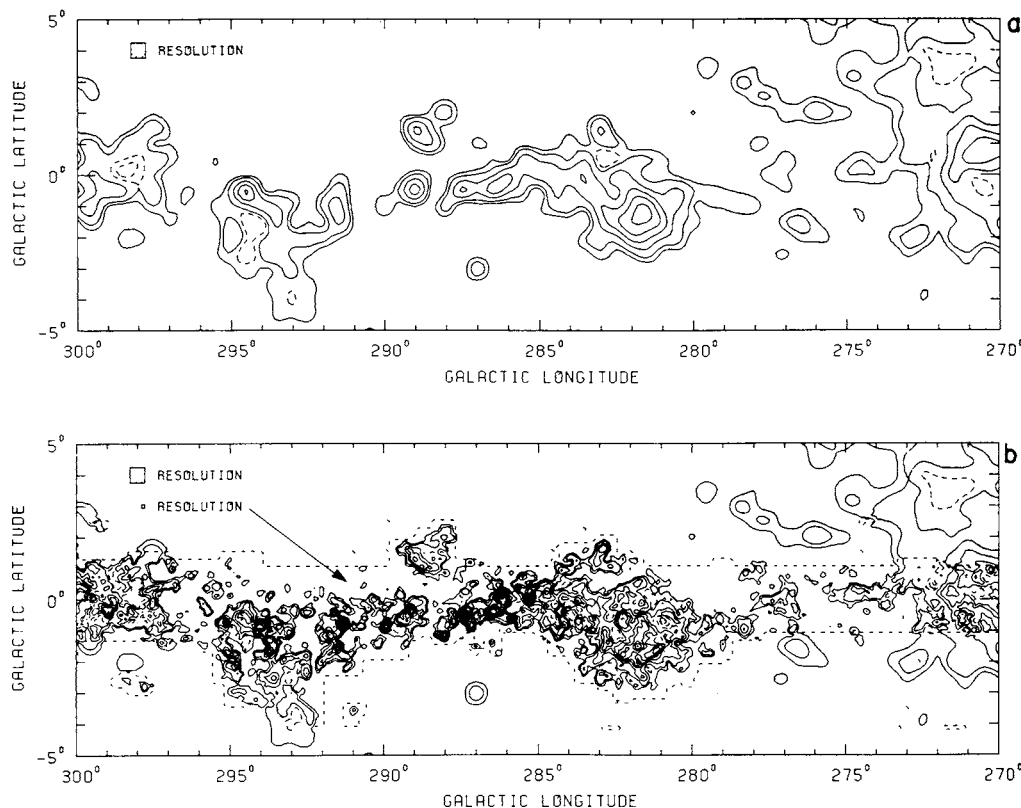
FIG. 3.—(a) Spatial map from clipped low-resolution data showing emission between $v = -100$ and $+100$ km s^{-1}. All spectral channels below 0.5 K ($\sim 3\ \sigma$) were set to zero before integrating. Contours are at 3, 6, 12, 18, ... K km s^{-1}. (b) Spatial map combining clipped full-resolution and clipped low-resolution data showing emission between $v = -100$ and $+100$ km s^{-1}. All spectral channels below 0.5 K ($\sim 3\ \sigma$) were set to zero before integrating. Contours are at 3, 6, 12, 18, ... K km s^{-1}.

extended emission in the upper left of the map originates in the inner Galaxy and is ignored here; for a discussion of this region see Bronfman 1986.)

III. RESULTS

a) Kinematics and Distribution of CO in the Carina Arm

i) The (l, v)-Diagram

In the fourth Galactic quadrant, material within the solar circle ($R_0 = 10$ kpc) is generally overtaking the Sun in its Galactic orbit, so radial velocities in the local standard of rest are negative; material beyond the solar circle, on the other hand, is falling behind, so radial velocities are positive. On the basis of the classic picture of the arm (§ I), we expect the signature of the Carina arm in the (l, v)-diagram to be a loop—the arm's near side traced at negative velocities between $l \approx 281°$ and 296°, its far side at positive velocities at longitudes greater than 281°, and the connecting tangent region near zero velocity at $\sim 281°$. Just such a signature stands out in the integrated (l, v)-map (Fig. 4); a schematic representation of the main features in the (l, v)-diagram is displayed in Figure 5. Because velocity crowding and noncircular motions affect somewhat the transformation from the (l, v)-plane to the Galactic plane (e.g., Burton 1971), a closer look at the Carina loop is desirable. Our intent is not to compare the observations with a numerical or analytical model of Galactic spiral structure, but rather to demonstrate the consistency of our inferred CO spiral structure with the known spiral structure of the Carina arm.

The near side of the arm lies along the high-velocity ridge between 280° and 300°, raising the possibility that velocity crowding, not the concentration of clouds to the arm, might be the main cause of the enhanced emission in this part of the (l, v)-diagram. While perhaps some chance line-of-sight overlaps of distinct molecular clouds near the terminal velocity do occur, much of the angular extent of the high-velocity ridge between 280° and 300° is spanned by two large CO concentrations, one from 284° to 289° and the other from 291° to 296° (see Fig. 4). Both of these are large ($\sim 7 \times 10^5\ M_\odot$) molecular cloud complexes associated with well-known optical Carina-arm tracers: the former complex with NGC 3372 (the η Carinae nebula), Gum 30, Gum 31, and IC 2581; and the latter with RCW 60, RCW 61, RCW 62, and NGC 3576 (Grabelsky 1985). Both complexes can, therefore, be placed in the near side of the Carina arm, and it is plausible by extension to attribute most of the high-velocity ridge emission between $\sim 284°$ and 300° to the near side of the Carina arm.

Between $l \approx 280°$ and 284°, the tangent region of the arm is marked near zero velocity by intense CO emission. A long path length through the arm lies in a narrow range of longitudes near the tangent, accounting for the high intensity of CO emission and the rapid increase in the velocity width as l increases from 280° to 284°. Some of this emission may be local, but the coincidence of the bright CO edge and the classic Carina tangent suggests that the local contribution is slight. Although it is obviously difficult to identify individual clouds or cloud complexes near the tangent owing to the heavy blending, four or five CO peaks kinematically near the tangent can be identified and associated with optical H II regions (e.g., G282.2−2.0,
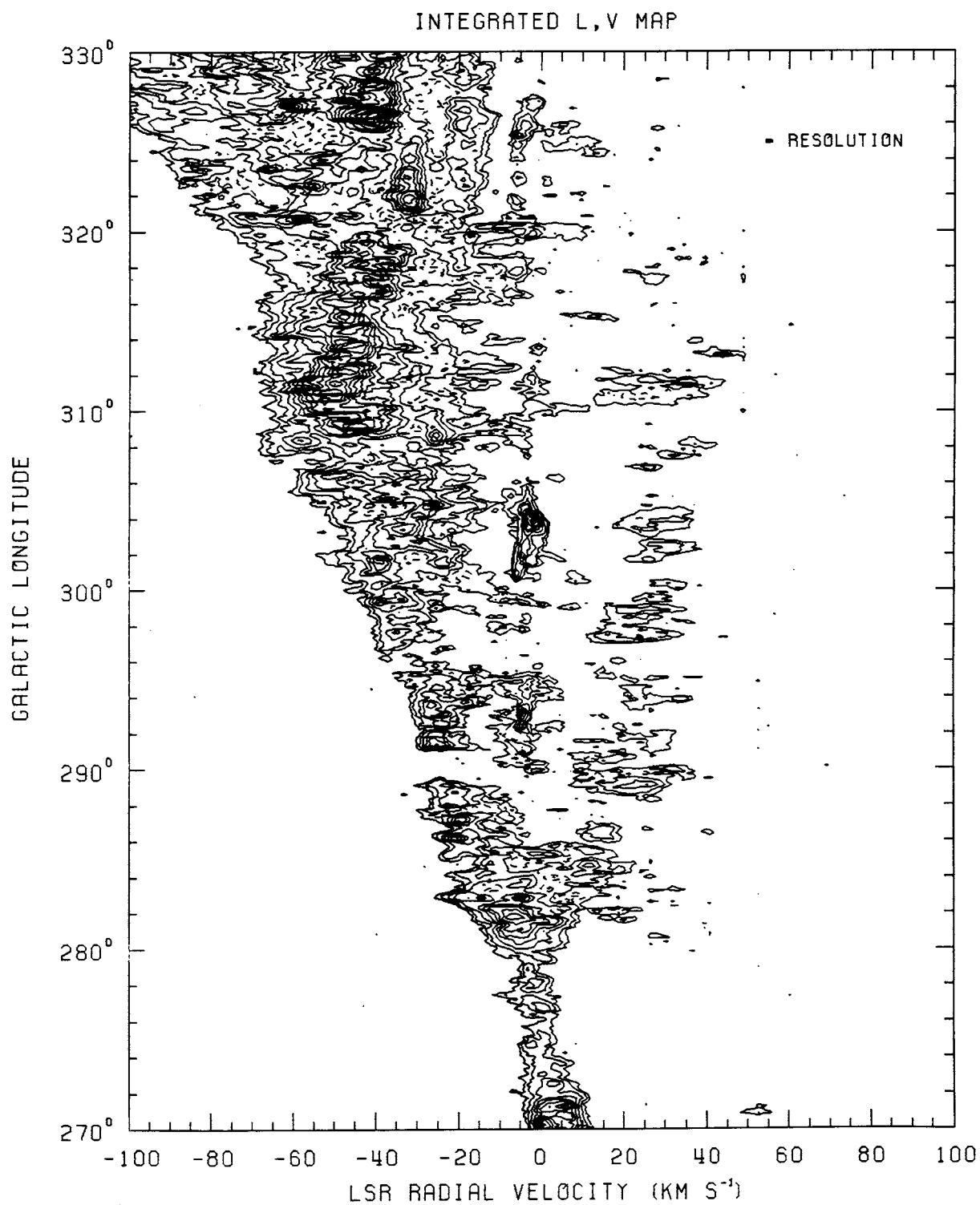
INTEGRATED L,V MAP

FIG. 4.—Full-resolution integrated (*l*, *v*)-diagram. The CO emission has been integrated over all latitudes where data were taken. Contours are at 0.35, 0.7, 1.4, 2.1, ... K deg.
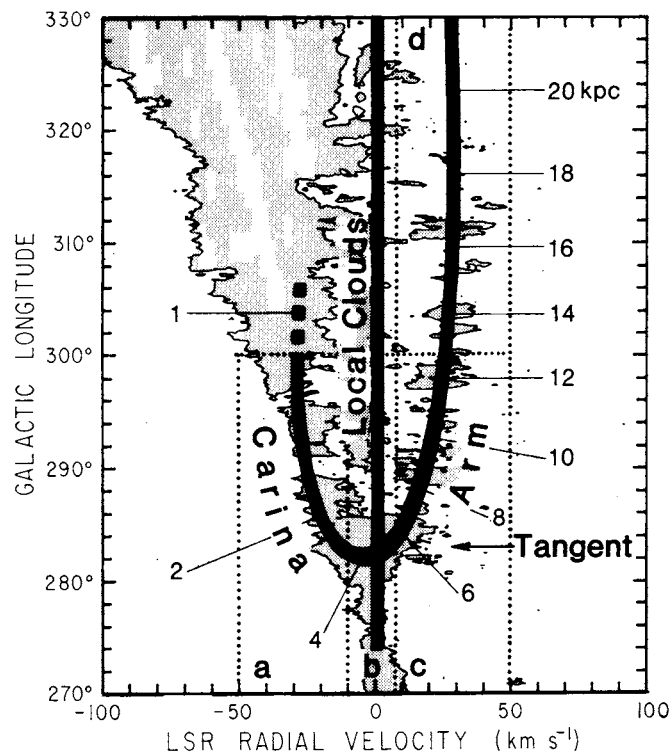
FIG. 5.—Key to discussion of Fig. 4 (§ IIIa[i]). Approximate heliocentric distances are marked off along the Carina arm. The dark lines are schematic and not derived from a model. The regions enclosed in dotted lines and labeled a, b, c, and d show the velocity limits used in the spatial maps of the near side, tangent region, and far side of the Carina arm (Figs. 7a–7d).

RCW 45, RCW 46, and RCW 47), which locate the optical tangent (Grabelsky 1985). The dip in CO emission just before $l = 280°$ is the nearly empty interarm region outward in galactocentric radius from the Carina arm tangent.

Above 280°, at positive velocities, the far side of the Carina arm extends away from the tangent point in an ordered sequence of molecular clouds. Because this part of the arm lies beyond the solar circle, kinematic distances are single-valued. A fairly sharp low-velocity edge above $\sim 284°$ marks the inner side of the arm; the nearly empty space between this edge and the lane near zero velocity is similar to the interarm gap observed between the local arm and the Perseus arm in the second quadrant (Cohen et al. 1980). As in the near arm, individual molecular clouds in the far arm between 280° and 300° coincide with previously known tracers of the Carina arm, including the very distant optical H II regions RCW 54a and NGC 3603 and the radio H II regions G282.0–1.2, H 58 and G298.2–0.3 (Grabelsky 1985). Beyond 300°, the arm extends to the top of the (l, v)-map; the speck at 329° and 30 km s^{-1} is real, a distant, $6 \times 10^5 M_\odot$ molecular cloud in the arm at 20 kpc. An even more distant cloud observed by Bronfman (1986) but not shown here extends the arm somewhat farther.

Down the center of the (l, v)-diagram, near zero velocity, is a narrow lane of emission which, although perhaps due in part to distant molecular clouds, is reasonably explained as local emission. Local emission is generally characterized by narrow lines and, as exemplified by the narrow-velocity component of the feature seen between $l = 293°$ and 295°, by a large latitude extent; in addition, at least one CO feature near $l = 294°.1$ can be identified with local dust (Grabelsky 1985). The general

weakness of this low-velocity emission between $l = 285°$ and 300°, however, correlates well with the generally low optical extinction in this part of the sky. The sparseness of the emission between the near and far sides in the (l, v)-diagram is evident also in the plane-of-the-sky map of the tangent region discussed in § IIIa(iii).

The good correspondence between simple kinematic picture and the optically derived picture of the Carina arm indicates that the loop in the (l, v)-diagram cannot be the result of noncircular motion, i.e., streaming. Our interpretation of the (l, v)-diagram is further supported by the coherence of the loop over nearly 60° of longitude, corresponding to ~ 20 kpc about the Galactic center. Except for the small amount of local gas, the region between the near and far sides of the arm in the (l, v)-diagram is remarkably free of emission. The gap is the interarm region interior to the Carina arm. With the possible exception of the Perseus arm (Cohen et al. 1980), no other CO spiral arm in the Galactic (l, v)-diagram exhibits such a sharp intensity drop at its inner edge—one of the main reasons the Carina loop stands out so conspicuously in the (l, v)-diagram.

ii) *Variation of Total Emission with Longitude*

The abrupt onset of the Carina tangent emission as the line of sight sweeps from below to 280° is illustrated especially well in Figure 6, which shows the emission from the full-resolution survey integrated over latitude and velocity, as a function of longitude. Plotting the total intensity of a continuum-like spiral tracer versus longitude is a classic method for locating the tangent directions of spiral arms (e.g., Mills 1959). In such an intensity-longitude, or $I(l)$, diagram, the tangent directions appear as upward steps in the intensity, and the ratio of brightness in the tangent direction to that in the preceding interarm direction is a good indication of the arm-interarm contrast of the spiral tracer. By integrating over velocity, streaming motions in the gas are eliminated as a possible cause of intensity variations. In the first quadrant, the CO $I(l)$ graph shows a typical ratio of tangent-to-interarm brightness of $\sim 2:1$ (Dame 1983), and similar ratios are seen in the fourth quadrant (Fig. 6) in the tangent directions of the Centaurus and Norma arms, at $l \approx 310°$ and 330°. For the Carina tangent at $l = 280°$, however, the ratio is much higher: $\sim 13:1$. (The nearby step down from 270° to 272°, entirely unrelated to the Carina arm, is the result of quite local clouds, as is shown by the high latitude extent of the emission in Fig. 2.)

This rather remarkable 13:1 step at the projected arm-interarm boundary is very likely due to a discontinuity in the density of molecular clouds, but two other possible explanations deserve consideration. First, the latitude coverage of the full-resolution survey fans out at about the same longitude as the step in the $I(l)$ graph, suggesting that the strength of the step might be an artifact of the sampling. This possibility was carefully checked by comparing $I(l)$ graphs produced from the low-resolution survey to the full-resolution $I(l)$ graph smoothed in longitude to $0°.5$. Since the smoothed, full-resolution $I(l)$ graph was found to be completely consistent with the low-resolution $I(l)$ graphs, and since the sampling of the low-resolution survey is uniform in l and b, the irregular sampling pattern of the full-resolution survey fails entirely to explain the high ratio of tangent-to-interarm brightness. Second, since CO emission from the tangent region of the Carina arm is kinematically indistinguishable from local, low-velocity CO emission, the strength of the step in the $I(l)$ graph might in part be due to contributions from local emission. Such
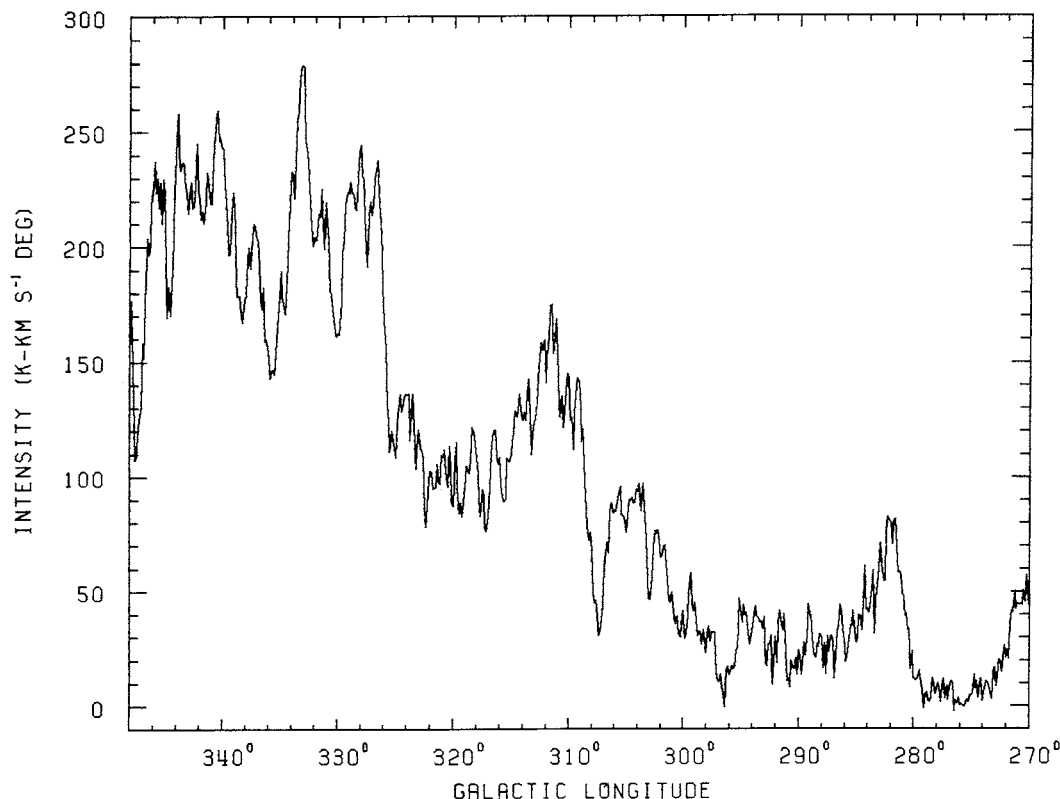
FIG. 6.—CO emission (full-resolution survey) integrated over all covered velocities and latitudes (in units of K km s^{-1} deg) as a function of longitude. Typical rms noise (1 σ) per longitude point is 2 K km s^{-1} deg.

contributions cannot be substantial, however, because no dark clouds are observed in the vicinity of the Carina tangent: O and B stars and optical H II regions are observed to at least 3 kpc at the Carina arm tangent (Graham 1970; Bigay *et al.* 1972; Georgelin 1975), and the absence of optical Population I material at lower longitudes than the tangent has a corresponding dip in the radio-continuum intensity.

We believe that the high ratio of tangent-to-interarm brightness is a true indication of the relative density of molecular clouds in the Carina arm and just beyond. This last explanation is by elimination the most plausible of the ones considered, leading to the conclusion that there is at least an order of magnitude more molecular gas in the Carina arm than in the interarm region ahead of the tangent. This finding is the strongest existing quantitative evidence that *molecular clouds in the Galaxy are largely confined to the spiral arms* (Cohen *et al.* 1980; Dame 1983) *and that CO is therefore an extremely good tracer of the large-scale structure of the system.*

iii) *The Spatial Maps*

To view the near and far sides and tangent region of the Carina arm on the plane of the sky, the survey spectra were integrated over the approximate velocity widths of these features as they appear in the integrated (l, v)-diagram (Fig. 4). The resultant spatial maps are shown in Figure 7; the velocity integration limits (vertical dotted lines in Fig. 5) are indicated on the maps. Below 300°, the spatial maps combine the full-resolution and low-resolution data; from 300° to 330° in longitude, only full-resolution data are available. In the discussion here the spatial maps are referred to according to the segment of the arm displayed, i.e., the near-side map (Fig. 7a); the

tangent-region map (Fig. 7b), which also contains some local emission; and the far-side maps (Figs. 7c and 7d).

Above 284°, the adopted near and far velocity bins are seen to contain nearly all of the Carina arm emission, but below 284°, where the near and far sides of the arm join the tangent, the velocity boundaries at −9 km s^{-1} (the inner edge of the near side), and at 7 km s^{-1} (the inner edge of the far side), define the velocity extent of the tangent region somewhat arbitrarily. These limits, however, evidently enclose most of the tangent emission, as a comparison of the tangent region map and the total emission spatial maps (Figs. 2 and 3) shows. Almost all the peaks between 280° and 285° in the total-emission map appear in the tangent-region map (exceptions are the peaks at $[l, b] = [283°, 1°5]$; $[284°25, 0°75]$; $[284°5, 0°5]$, the first two seen in the near-side map, the third in the far-side map). The abrupt onset of the tangent emission, prominent in the total-emission map, is equally evident in the tangent-region map. Although the total-emission map is more intense than the tangent-region map, the complicated structure of the emission between $l = 280°$ and 285° is similar in both, because the small velocity interval of the tangent region corresponds to a fairly long segment of the arm.

Two other characteristics of the emission in the tangent-region map should be noted: First, the wide-latitude emission between 270° and 275° is almost completely contained in the low-velocity bin of the tangent-region map (compare the near- and far-side and tangent-region maps), supporting our earlier assertion that this emission is local in origin. Second, the emission between the near and far sides of the arm above 285° in the (l, v)-diagram is weak when viewed in the plane of the sky (compare the tangent-region map with the near-side and far-
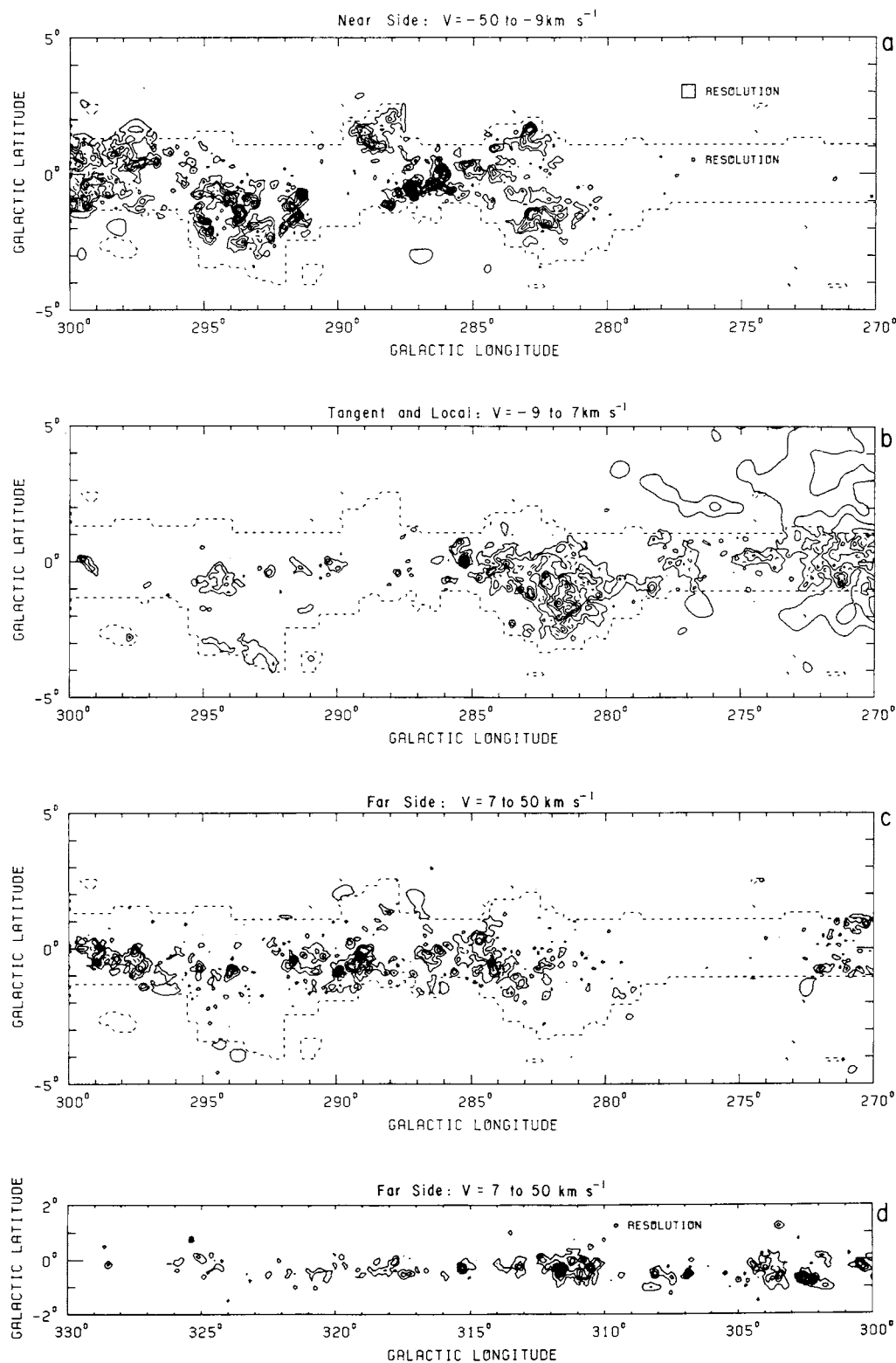
FIG. 7.—Spatial maps of CO emission integrated over the indicated velocity ranges. (a) Near side of the Carina arm; (b) tangent region; (c)-(d) far side. Full-resolution data are shown inside the dotted lines in the maps covering $l = 270°-300°$ (a)-(c); low-resolution data are shown beyond the dotted lines. At $l > 300°$, only full-resolution data are available. The contour interval is 5 K km s^{-1}.

side maps between 285° and 300°), supporting our assertion that the interarm region interior to the Carina arm is comparatively free of molecular clouds.

The spatial map of the near side (Fig. 7a) is evidently characterized by fairly well defined molecular clouds or cloud complexes between 284° and 296°. The complex structure with several strong CO peaks between 284° and 289° near the Galactic plane is a single cloud complex, as noted in § IIIa(i), associated with the η Carinae nebula, the brightest optical feature in the Carina arm. The emission between 291° and 296° comprises a large cloud complex (also mentioned above) associated with a group of H II regions, including the optically prominent Carina arm objects RCW 62 and NGC 3576. Between 280° and 284°, below the Galactic equator, where the near side joins the tangent (compare Figs. 7a and 7b), the velocity boundary between the near-side and tangent-region maps may artificially partition some of the emission, and identification of individual clouds in this region is less certain. The total latitude extent of the near side is 3°–4°, corresponding to a total thickness of ∼160–210 pc, on the assumption of an average distance of 3 kpc to this part of the arm.

In the far side of the arm (Figs. 7c and 7d), most of the emission is concentrated somewhat below the Galactic equator. As the longitude increases, it is apparent that the extent in latitude progressively decreases simply from the increase in distance—an unambiguous demonstration of the "latitude effect" much harder to demonstrate with 21 cm clouds.

iv) Distribution about the Galactic Plane

Since no kinematic distance ambiguity exists for emission beyond the solar circle, a unique distance z from the Galactic plane may be assigned to the CO at each observed l, b, and v when $R > R_0$, and the distribution of molecular material about the plane can be readily determined. In this section, the z-position, thickness, and surface and volume density of the disk of molecular clouds beyond the solar circle are derived as functions of R on the assumption of circular rotation about the Galactic center.

The spiral nature of the Carina arm, and an indication of how the molecular gas in it departs from strict axial symmetry about the Galactic center, are illustrated in Figure 8, where, on the assumption of a flat rotation curve with $V = 250$ km s^{-1}, galactocentric rings are shown against an outline of our (l, v)-diagram. (The rings retain their $[l, v]$-shape and galactocentric spacing with the revised values of R_0 and V_0; each is reduced by ∼1.5 kpc in radius.) The opening out of the Carina arm with increasing longitude is obvious, particularly between $l \approx 280°$ and 310°. It is also apparent that individual clouds in the arm have internal velocities that, if interpreted "kinematically," spread them out over a few kiloparsecs in galactocentric radius. Because each (l, b, v) is considered a distinct spatial position and nonaxisymmetric structure is ignored in our analysis, the arm will be largely washed out in the following treatment. Yet, as we show, by considering a restricted range of longitudes the arm and interarm regions can easily be distinguished.

To convert the observed CO luminosity at each position to density, the integrated emission, $W(\mathrm{CO}) \equiv \int T_R \, dv$, is assumed to be proportional to the column density of molecular hydrogen $N(\mathrm{H}_2)$. Even though the CO line is typically optically thick in molecular clouds, $W(\mathrm{CO})$ has been shown empirically to be a good tracer of molecular cloud mass (e.g., Lebrun et al. 1983;
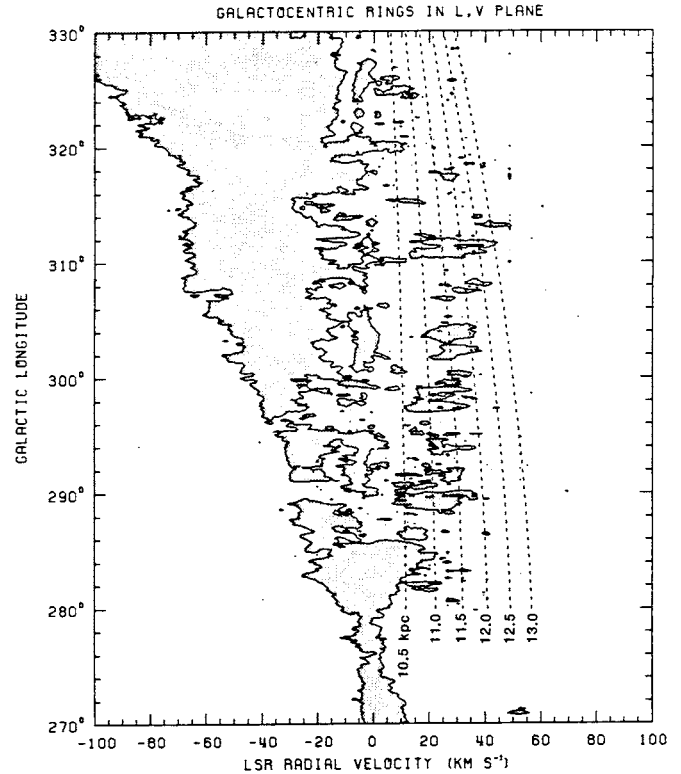

FIG. 8.—Galactocentric rings of radii 10.5, 11.0, 11.5, 12.0, 12.5, and 13.0 kpc are shown transformed to the (l, v)-plane using a flat rotation curve, $V(R) = 250$ km s^{-1}. The shaded region outlines the data. For $R_0 = 8.5$ kpc and $V_0 = 220$ km s^{-1}, the rings retain their (l, v)-shape, and each radius is reduced by ∼1.5 kpc.

Bloemen et al. 1986; Sanders, Solomon, and Scoville 1984, hereafter SSS), presumably because most clouds are composed of many optically thick elements or condensations which overlap little in the line of sight or in velocity (or both). We adopt here the ratio derived by Bloemen et al. from a comparison of CO, H I, and γ-ray data toward the inner Galaxy in the first quadrant and the outer Galaxy in the fourth:

$$N(\mathrm{H}_2)/W(\mathrm{CO}) = 2.8 \times 10^{20} \text{ cm}^{-2} \text{ (K km s}^{-1})^{-1} . \quad (1)$$

If expression (1) is written in the differential form, $dN(\mathrm{H}_2) = 2.8 \times 10^{20} T_R \, dv$ (cm^{-2}), then the density at any point (R, z) can be written

$$\rho(R, z) = 6.17 T_R(l, b, v)| \, dr/dv |^{-1} \, M_\odot \text{ pc}^{-3} , \quad (2)$$

where T_R is the CO line temperature; R and z (for $R > R_0$) are uniquely determined by l, b, and v (in km s^{-1}), r is the kinematic distance to the point in parsecs, and the mean molecular weight per H_2 molecule (including He) has been taken to be $2.76 m_\mathrm{H}$ (Allen 1973). The factor $| \, dr/dv |^{-1}$ can be calculated from the rotation curve using the expression for the observed radial velocity due to differential Galactic rotation, $v_\mathrm{LSR} = R_0[\omega(R) - \omega(R_0)] \sin l \cos b$, where $\omega(R)$ is the angular velocity at radius R. A flat rotation curve $[V(R) = 250$ km s$^{-1}]$ was used as a reasonable first approximation and to facilitate comparison of the CO results with the H I results of Henderson et al. (HJK). The projected surface density $\sigma(R)$ is just $\int \rho(R, z) dz$, where the integral runs over all z. In this analysis, the computed densities at each point (l, b, v) between $l = 280°$ and 335°, weighted according to the respective volume ele-
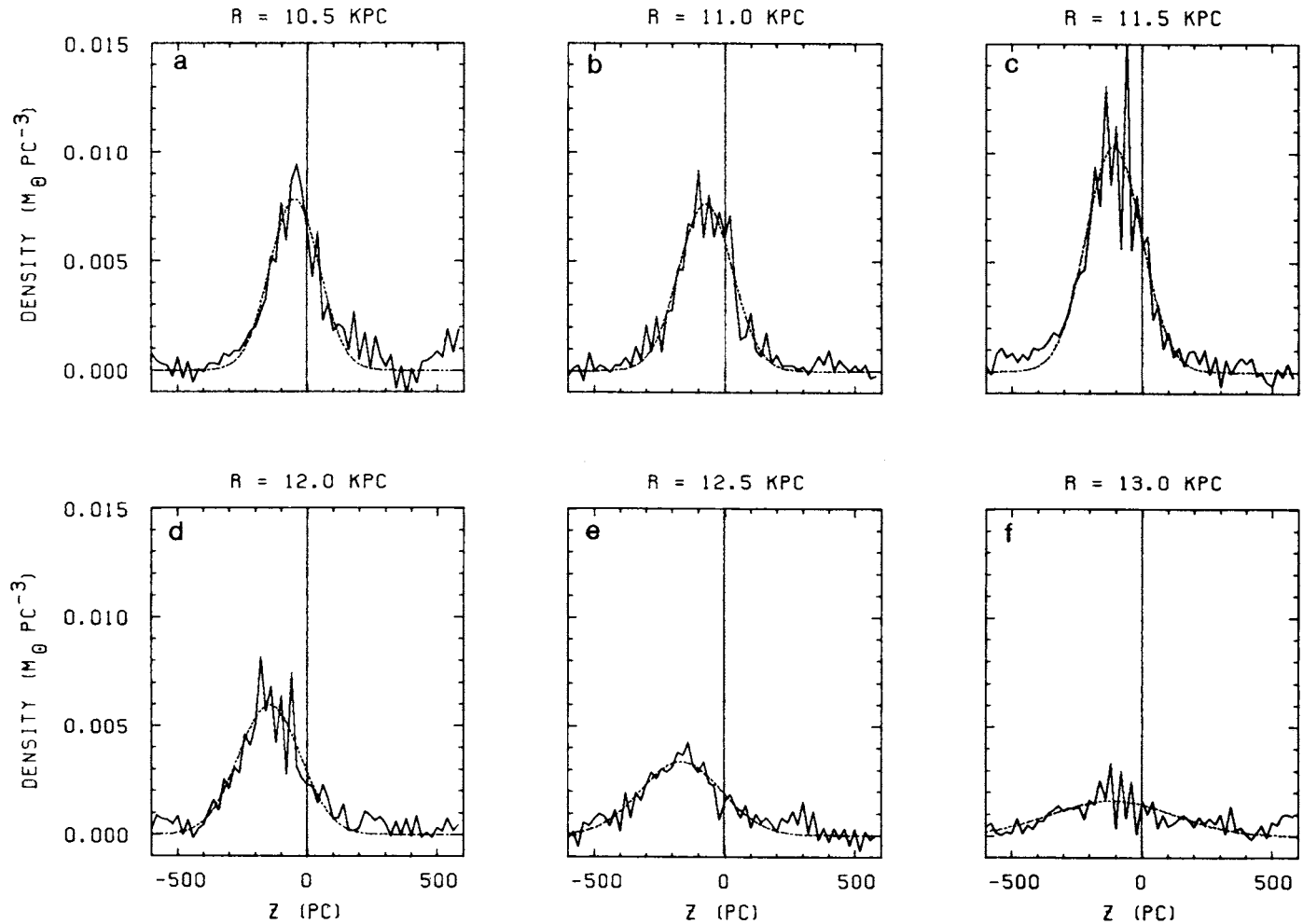
FIG. 9.—Volume density of H_2 as a function of vertical distance z from the Galactic plane at fixed galactocentric radii beyond the solar circle. Each point in z represents an average over 20 pc bins in z and 500 pc rings in R. *Solid line*, data; *dotted line*, best-fit Gaussian. The label above each plot indicates the galactocentric radius of the center of the ring.

ments, were summed in bins in R and z, yielding a sampled mass per bin. Dividing the total mass sampled by the total volume sampled in a given bin yields the average density for the bin.

The results for $\rho(R, z)$ plotted as a function of z at fixed R, starting at 10.5 kpc, are indicated by the solid line in Figure 9. At each radius, a Gaussian

$$\rho(z) = \rho_0 \exp\left[-(z - z_0)^2 \frac{\ln 2}{z_{1/2}^2}\right] \tag{3}$$

was fitted to the data and three free parameters determined (see

Table 1): ρ_0 [denoted $\rho(\langle z_0 \rangle)$], the peak density of the Gaussian; z_0, the z-displacement of the peak; and $z_{1/2}$, the half-thickness at half the peak density. The fits (*dotted lines*) are evidently fairly good representations of the actual distribution at each radius. Table 1 gives the parameters from the fits, the H_2 surface density based on the fits, and, for comparison, the surface density measured directly from the area under the solid (data) curves. The CO midplane, layer thickness, and surface density are plotted as a function of radius in Figure 10.

Between the solar circle (10 kpc) and 12.5 kpc, the mean of the distribution dips below the plane, reaching a maximum displacement of $z = -167$ pc. The half-thickness of the layer

TABLE 1

z-DISTRIBUTION OF H_2 IN THE CARINA ARM BEYOND THE SOLAR CIRCLE

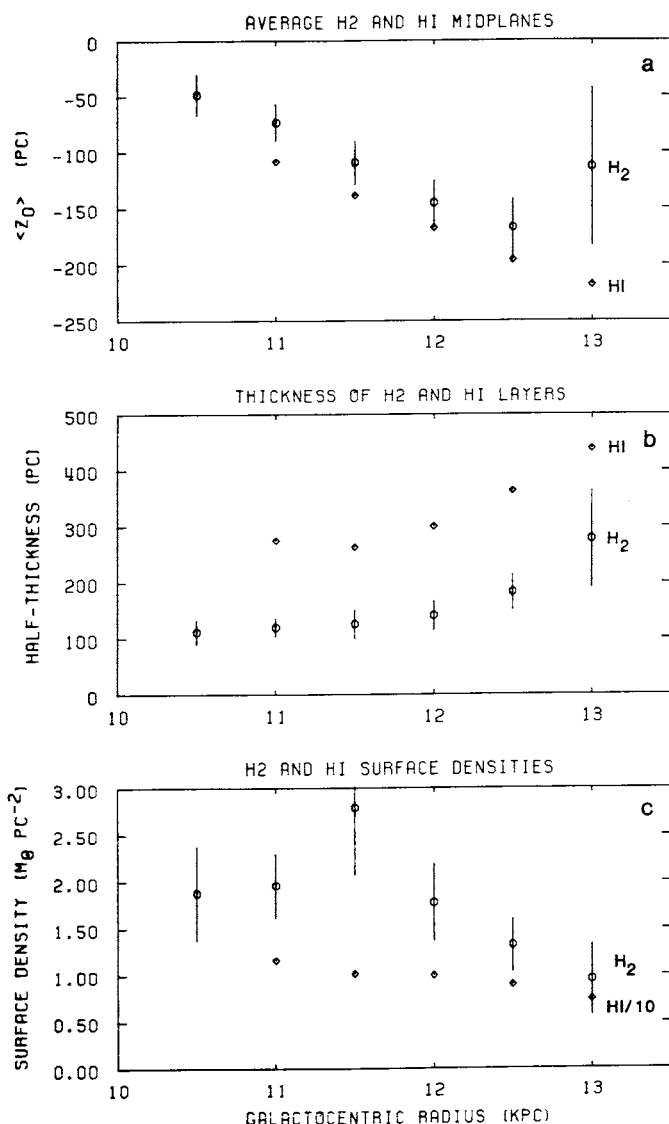| Radius (kpc)	$\langle z_0 \rangle$ (pc)	$z_{1/2}$ (pc)	$\rho(\langle z_0 \rangle)$ ($M_\odot$ pc^{-3})	σ_{fit} ($M_\odot$ pc^{-2})	$\sigma_{measured}$ ($M_\odot$ pc^{-2})
10.5	-48 ± 18	112 ± 21	0.0078 ± 0.0015	1.88 ± 0.50	2.18 ± 0.06
11.0	-73 ± 16	120 ± 16	0.0077 ± 0.0008	1.96 ± 0.34	2.11 ± 0.06
11.5	-109 ± 19	126 ± 25	0.0104 ± 0.0017	2.79 ± 0.71	3.00 ± 0.04
12.0	-145 ± 20	141 ± 26	0.0060 ± 0.0008	1.78 ± 0.41	2.02 ± 0.04
12.5	-167 ± 25	182 ± 31	0.0034 ± 0.0004	1.32 ± 0.28	1.40 ± 0.04
13.0	-114 ± 70	277 ± 86	0.0017 ± 0.0014	0.95 ± 0.38	1.02 ± 0.04

FIG. 10.—Parameters of the vertical distributions of H_2 (*circles*) and H I (*diamonds*) in the outer Galaxy between $R = 10.5$ and 13.0 kpc: (*a*) average midplanes, z_0; (*b*) thicknesses, $z_{1/2}$; and (*c*) surface densities, σ (the H I surface density is divided by 10 to fit on the same scale as the H_2 surface density). For H_2 the parameters are taken from Gaussian fits (Fig. 9, *dotted lines*) to the data (*solid lines*). Error bars on the H_2 parameters represent the formal errors from the fit in each ring (of average radius R) multiplied by a galactocentric-dependent correction factor $\sqrt{N}$, where N is the number of resolution elements (*l*, *b*, and *v*) subtended by a typical cloud (50 pc diameter, 6 km s^{-1} wide) at the average distance to the ring; the correction factor accounts (approximately) for correlation of the data over the emission volume of discrete molecular clouds. No attempt has been made to estimate the errors on the H I parameters because of the uncertainty of the true form of the H I layer distribution.

grows with increasing radius. By 13 kpc, very little molecular hydrogen is observed, and uncertainties are therefore large (Fig. 9 and Table 1). The surface density of H_2 beyond the solar circle is known to be generally smaller than in the inner Galaxy (e.g., SSS) and drops off with increasing radius beyond R_0. Between $l = 280°$ and 335°, however, our results show a peak in $\sigma(H_2)$ at $R = 11.5$ kpc, probably caused by the three or four large molecular clouds between 290° and 320° which straddle the 11.5 kpc ring (Fig. 8). The H_2 surface density at

the 11.5 kpc peak is only a factor of ~ 4 below that of the peak of the "molecular ring" in the inner Galaxy determined by Dame (1983) by fitting an axisymmetric model to the Columbia CO survey of the first quadrant. If our 11.5 kpc peak is representative of the surface density in the Carina arm, it follows that a single spiral arm may account for a significant fraction of the H_2 surface density observed in the interior region of the Galaxy.

Between longitudes 290° and 310°, the two rings at 10.5 kpc and 11.5 kpc (Fig. 8) can be used to determine the arm-interarm contrast, specifically, the ratio of molecular surface densities. We find that $\sigma(H_2) = 1.1$ $M_\odot$ pc^{-2} at 10.5 kpc, and 4.9 $M_\odot$ pc^{-2} at 11.5 kpc, for an arm-interarm surface density ratio of ~ 4.5 to 1. Because the 11.5 kpc ring smears out the arm somewhat, the actual contrast is probably somewhat higher—closer to the 13:1 contrast in the doubly integrated intensity at the tangent point relative to that just beyond (§ IIIa[ii]).

Finally, the total molecular mass between 280° and 335° in *l* and 10.25 kpc and 13.25 kpc in R may be obtained by simply multiplying the surface density of each ring segment by the area of the segment and summing. The result using the surface densities from the fits is 1.0×10^8 $M_\odot$, while the result from the measured surface densities (the areas under the solid curves in Fig. 9) is 1.1×10^8 $M_\odot$.

b) Comparison with H I

In this section we compare the large-scale distributions of H_2 and H I. Similar comparisons for the first quadrant show that the H_2 and H I generally share the same large-scale kinematics (e.g., Dame 1983; SSS) and appear to offer similar pictures of spiral structure (Cohen *et al.* 1980; Dame 1983), although the CO appears more confined to the spiral arms (Dame 1983). The H I data used to produce the maps discussed in this section are from a neutral hydrogen survey of the southern Milky Way made with the Parkes 18 m telescope (HJK), kindly provided on a magnetic tape by Dr. Frank Kerr.

i) The (l, v)-Diagrams

Figure 11 is the H I (*l*, *v*)-map integrated for $|b| \leq 2°$, covering the same region of (*l*, *v*)-space shown in the CO (*l*, *v*)-map in Figure 4. As in the first quadrant (e.g., Burton and Gordon 1978; Dame 1983; SSS), the CO and H I terminal velocity curves are quite similar. For example, between $l = 315°$ and 318°, the ridge becomes almost vertical in both CO and H I; at 313°, a slight positive velocity indentation is flanked on either side (in *l*) by two negative velocity bumps in both the CO and H I high velocity ridges. These and other apparent parallels of the CO and H I terminal velocity curves suggest that on the scale of a few hundred parsecs, the kinematics of molecular and atomic gas do not differ greatly.

Quantitative evidence of this conclusion is provided by a comparison of the emission-weighted mean velocities of CO and H I along the high-velocity ridges. For the comparison we define the mean velocity of the high-velocity ridge of species X (CO or H I) at longitude *l*, $\langle v(l)_{HVR} \rangle_X$, as

$$\langle v(l)_{HVR} \rangle_X = \int v_X(l) T_X(l, v) dv \bigg/ \int T_X(l, v) dv , \qquad (4)$$

where the integrals extend over ± 25 km s^{-1} of the assumed rotation curve at the given longitude and, before integrating, the CO data are smoothed in *l* to the resolution of the Parkes survey. The difference between these mean velocities,
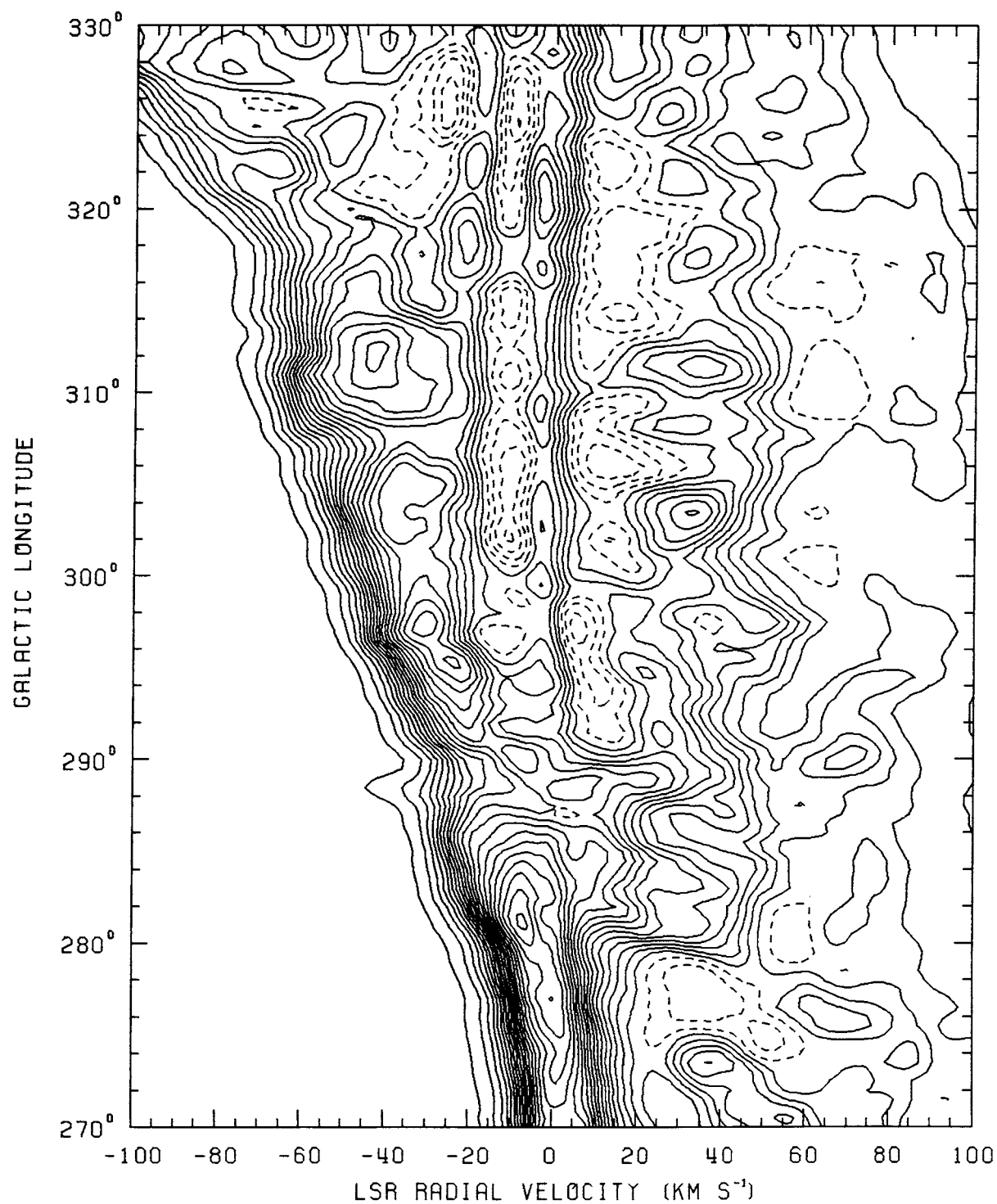
FIG. 11.—Longitude-velocity map of H I emission integrated in latitude from $b = +2°$ to $-2°$. Data from the Parkes 18 m 21 cm survey of the southern Milky Way (HJK) are in units of brightness temperature. Contour interval is 25 K deg.

$\Delta\langle v_{\mathrm{HVR}}(l)\rangle$, where

$$\Delta\langle v(l)_{\mathrm{HVR}}\rangle \equiv \langle v(l)_{\mathrm{HVR}}\rangle_{\mathrm{CO}} - \langle v(l)_{\mathrm{HVR}}\rangle_{\mathrm{HI}}, \qquad (5)$$

should be approximately independent of the rotation curve used. Figure 12 shows the velocity residuals plotted against longitude; to demonstrate the relative insensitivity to the rotation curve, the residuals were calculated using both the Burton and Gordon (1978) rotation curve [*solid line for* $\Delta\langle v(l)_{\mathrm{HVR}}\rangle$] and a simple straight line in the (l, v)-plane from $v = -85$ km s^{-1}, $l = 330°$, to 0 km s^{-1}, 270° [*dotted line for* $\Delta\langle v(l)_{\mathrm{HVR}}\rangle$]. A large discrepancy between the CO and H I terminal velocities appears near $l = 290°$, the longitude of a conspicuous gap in the CO high-velocity ridge, but because there is no CO emission in this region, $\langle v(l)_{\mathrm{HVR}}\rangle_{\mathrm{CO}}$ is poorly defined. Other than in this direction, however, the magnitude of $\Delta\langle v(l)_{\mathrm{HVR}}\rangle$ is generally less than 5 km s^{-1}, quantifying both the agreement of the CO and H I terminal velocities and the similarity of the large-scale (≥ 1 kpc) kinematics of the two species. (On a smaller scale, say 100 pc or less, significant differences between the kinematics of H I and H$_2$ are not ruled out by this demonstration; they can—and probably do—occur.)

Neutral hydrogen beyond the solar circle, at positive velocities in Figure 11, is easily followed to higher velocity than the CO, but the strongest H I feature remains the Carina arm. The resemblance of the CO and H I pictures of the outer Carina arm is striking when the CO (l, v)-diagram is compared to a "clipped" H I (l, v)-diagram (produced by setting all spectral channels below 50 K to zero before integrating in latitude). In the clipped map (Fig. 13), the strongest H I features are emphasized. Nearly every H I peak in the outer Carina arm has a corresponding peak or complex of peaks in the CO map, each of these CO peaks being a giant molecular cloud (Grabelsky 1985). Note especially the features at: $(l, v) \approx (303°, 32$ km s$^{-1})$; $(311°, 35$ km s$^{-1})$; and $(329°, 30$ km s$^{-1})$. Generally, the shapes of these objects are similar in CO and H I; the main compact features in neutral hydrogen, then, appear to be fairly closely associated with giant molecular clouds.

The tangent region is a strong H I feature, but it is not continuously connected to the far side of the arm. The uncertainty of a connection is due partly to the apparent continuity of the far side at $l > 280°$ with the H I at about the same velocity at $l < 280°$ (e.g., the concentration at $[l, v] = [273°, 35$ km s$^{-1}]$ in Fig. 11). HJK reexamined H I in the outer Galaxy by considering emission only at kinematically determined galactocentric radii greater than 11 kpc; intentionally omitting the inner Galaxy from their analysis to avoid the problem of kinematic distance ambiguity, they excluded the tangent region and interpreted the far side as continuing to $l \approx 265°$ (inferred from their map of H I projected surface density in the Galactic plane). Two properties of the H I (l, v)-map (especially the clipped version) do suggest that the far side of the arm does not continue to longitudes less than 280°. First, between $v = 15$ and 45 km s^{-1}, a sudden rise of the H I contours in the direction of increasing l between 279° and 280° is uncharacteristic of the gentler slopes of the contours between the H I concentrations at $l > 280°$ in the far side. Second, a
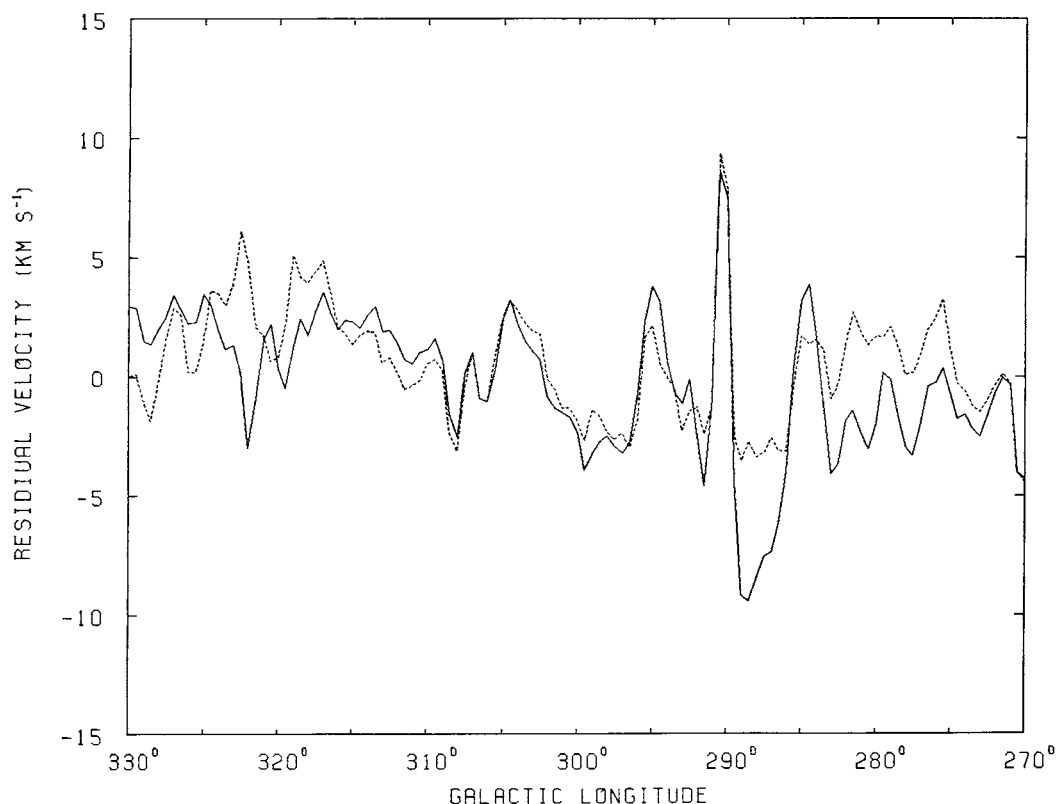

FIG. 12.—Comparison of CO and H I high-velocity ridges. The difference between the mean CO high-velocity ridge and the mean H I high-velocity ridge is plotted. The mean high-velocity ridge at each l is defined as the velocity-weighted emission (CO or H I) within ± 25 km s^{-1} of the expected rotation-curve velocity at that l. *Solid line*, result using the rotation curve of Burton and Gordon (1978); *dotted line*, result using a simple straight line drawn in the (l, v)-plane from $v = -85$ km s^{-1}, $l = 330°$, to $v = 0$ km s^{-1}, $l = 270°$.
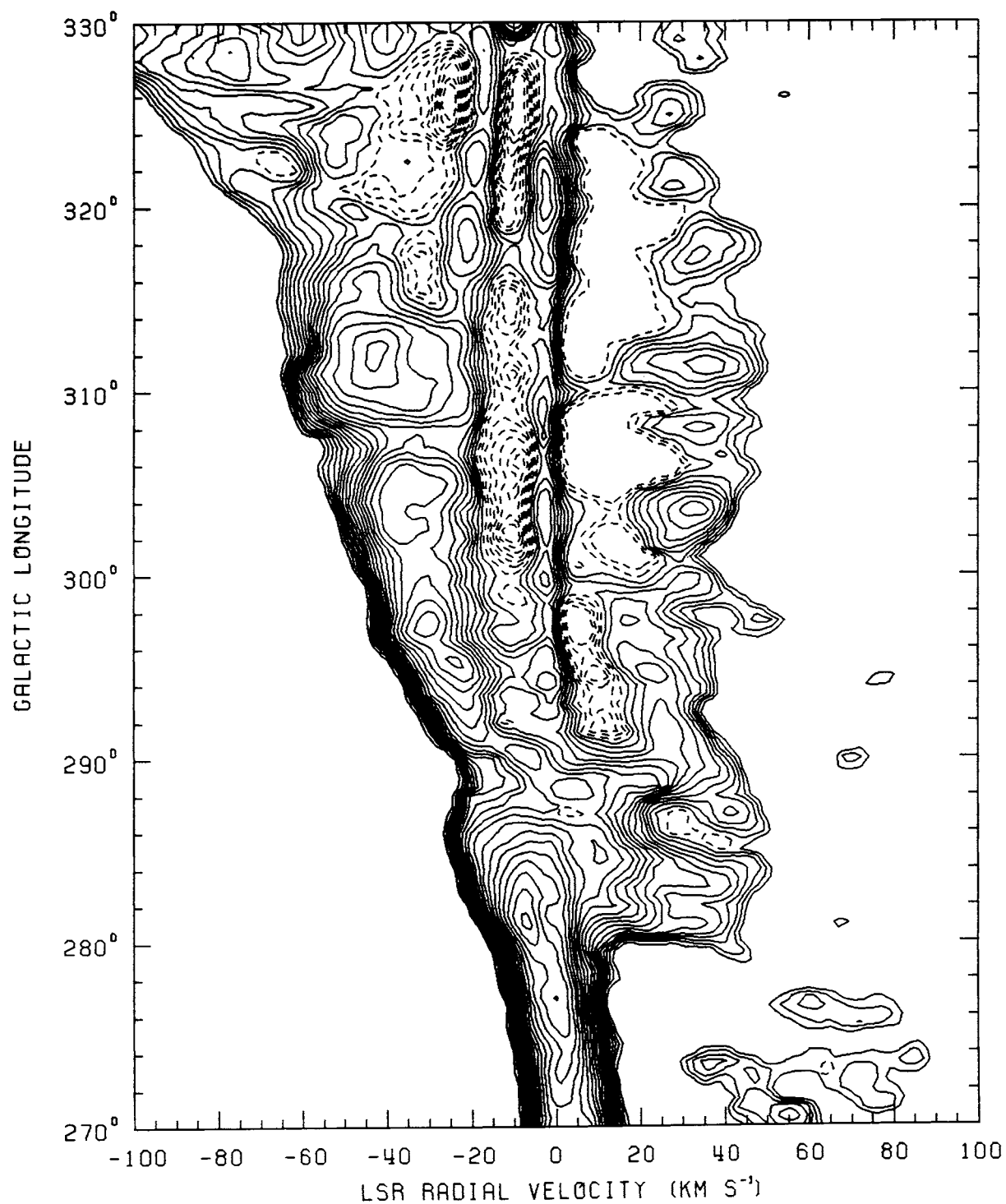
FIG. 13.—Longitude-velocity map of clipped H I emission integrated in latitude from $b = +2°$ to $-2°$. All spectral channels with $T_b < 50$ K were set to zero before integration. Contour interval is 25 K deg.

deep trough in the emission centered at $(l, v) \approx (277°, 35$ km s$^{-1})$, which separates the far side at $l > 280°$ from the feature at $(273°, 35$ km s$^{-1})$, is not representative of the shallower depressions between the other far-side concentrations. The best evidence against the interpretation that the far side of the Carina arm extends to longitudes less than 280°, however, comes from the CO (l, v)-diagram (Fig. 4), which demonstrates the strength of the tangent and the clear continuity of the near and far sides with the tangent. Without the CO data, extension of the H I counterpart of the far side to $l < 280°$ could not be convincingly ruled out.

An interesting feature in the near side of the arm is the 2° wide gap in the CO high-velocity ridge centered near $l = 290°$. This gap is most readily interpreted as simply the space between two large molecular clouds or cloud complexes. In H I, a corresponding feature near 290° appears as a shift of the high-velocity ridge toward more positive velocities and a shallower increase in intensity of the ridge with velocity than at neighboring longitudes. Humphreys and Kerr (1974) interpreted the detour of the H I high-velocity ridge as evidence for a large-scale shock at the inner edge of the Carina arm, but if the CO gap is merely the space between successive large molecular objects and the H I follows the CO, then another interpretation is possible: there may simply be an absence of neutral hydrogen near the terminal velocity at this longitude. The possibility that a large-scale disturbance is responsible for the absence of CO and (perhaps) H I in this direction, however, cannot at present be ruled out; the region merits detailed study. Aside from such indirect evidence for correlation of H I and CO in the near side, the general strength of the H I high-velocity ridge makes tracing the near side of the Carina arm in the H I (l, v)-map difficult and, perhaps more than any other aspect of the H I emission, masks the Carina "loop" in the H I (l, v)-map.

ii) The Spatial Maps

The H I spatial map of the total emission between -100 and 100 km s^{-1} (Fig. 14) is qualitatively similar to the CO total emission map (Fig. 2). The tangent region is recognizable, as is the general latitude shape of the layer at $l > 280°$, even though most individual peaks are washed out. The more diffuse appearance of the H I relative to the CO is due only partly to the lower spatial resolution of the 21 cm observations, since spatial maps of our CO data smoothed to the 48' resolution of the Parkes survey (not shown here) display more structure than is evident in the H I.

H I spatial maps of the near side, tangent region, and far side of the arm made with the same velocity windows used for the CO spatial maps are shown in Figure 15. The tangent region map (Fig. 15b) shows the H I counterpart to the CO tangent, although the former does not exhibit so abrupt an outer edge at $l \approx 280°$ as the latter, nor is the interarm region at $l > 285°$ so empty in H I as in CO. In the near side of the arm, where the high-velocity ridge dominates the H I (l, v)-diagram, an apparent H I concentration can be seen in the spatial map (Fig. 15a) between $l \approx 280°$ and 288°; the sudden shift of the H I high-velocity ridge toward positive velocities near $l = 290°$, noted above, is marked here by a relative trough in the spatial map between $l = 288°$ and 290°, supporting the interpretation of the notch in the high-velocity ridge as a true absence of material. In the far-side spatial maps (Figs. 15c and 15d), although the latitude extent of the H I is everywhere greater than the CO, the projected thickness of the H I layer generally decreases from 280° to 330°, and, like the CO and H I (l, v)-maps, these spatial maps show a close correlation between H I concentrations and the CO peaks. A strong H I feature in the far-side map at $(l, b) \approx (273°, -1°5)$ might be interpreted as an extension of the far side of the Carina arm to $l < 280°$. The depression of the contours separating this feature from the emission that begins abruptly at $l \approx 280°$, however, is deeper than the troughs between any of the H I concentrations farther along the far side of the arm $(l > 280°)$, suggesting (as the $[l, v]$-map did) that the far side of the Carina arm does not connect with any feature below $l \approx 280°$ in the outer Galaxy.

iii) Distribution about the Galactic Plane

The distribution of H I about the Galactic plane in the outer Galaxy was also reinvestigated by HJK. In the southern Milky Way, their results, in agreement with earlier findings, show that the displacement of the H I midplane is below the $b = 0°$ plane and increases with increasing distance from the Galactic center, reaching an extreme value of $z = -850$ pc at $R \approx 17$ kpc and a galactocentric azimuth of 260° (where 0° coincides with $l = 0°$ and the angle increases counterclockwise). The width of the layer increases outward as well, attaining a "half-thickness" (defined by HJK as the width about the midplane within which the projected surface density equals half the total projected surface density) of ~ 2 kpc near the outer edge of the Galaxy.

Most of the results of HJK are presented in the form of contour maps in the Galactic plane, making direct comparison with our CO data in the overlapping region (§ IIIa[iv]) some-
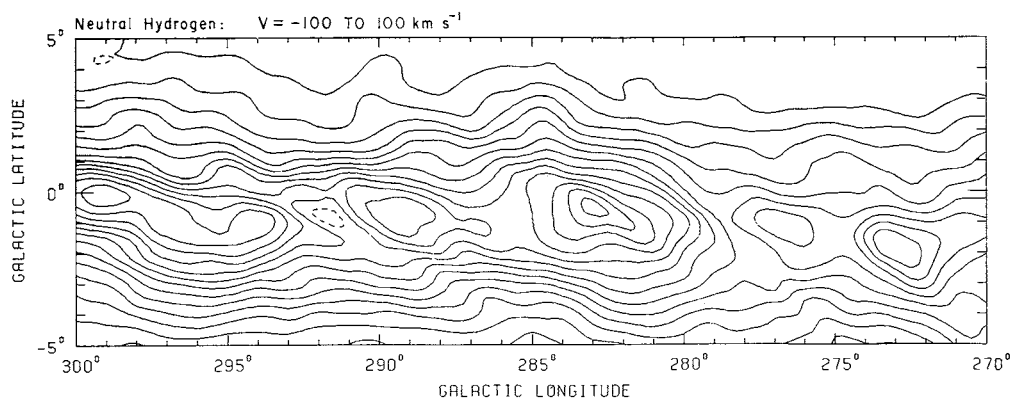

Fig. 14.—Spatial map of H I emission integrated from -100 to $+100$ km s^{-1}. Contours are at 500, 2000, 4000, 6000, ... K km s^{-1}.
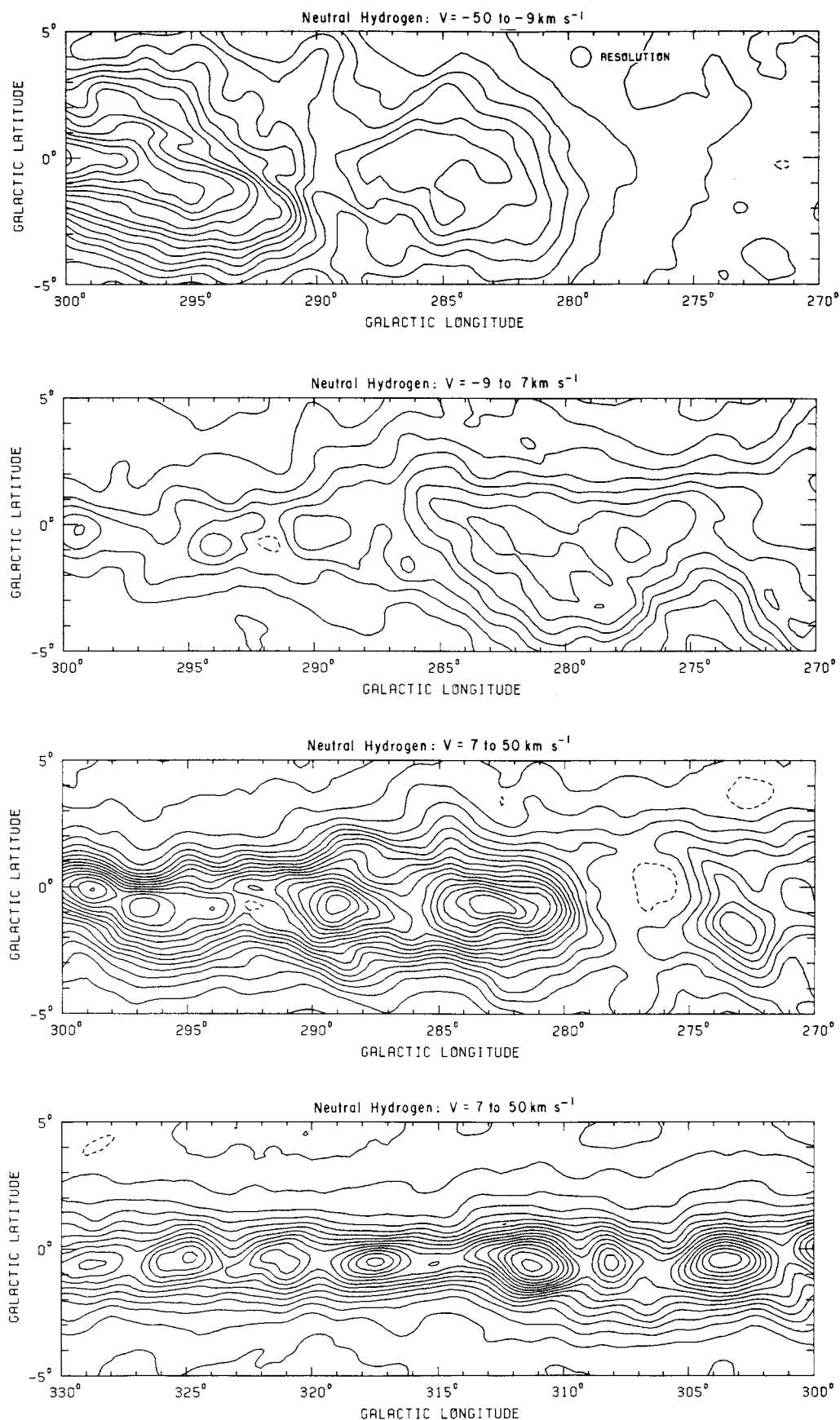
FIG. 15.—Spatial maps of H I emission in the Carina arm integrated over the indicated velocity ranges. These maps correspond to the CO spatial maps of the near side, tangent region, and far side of the Carina arm (Figs. 7a–7d). Contours are at 100, 200, 400, 600, ... K km s⁻¹.
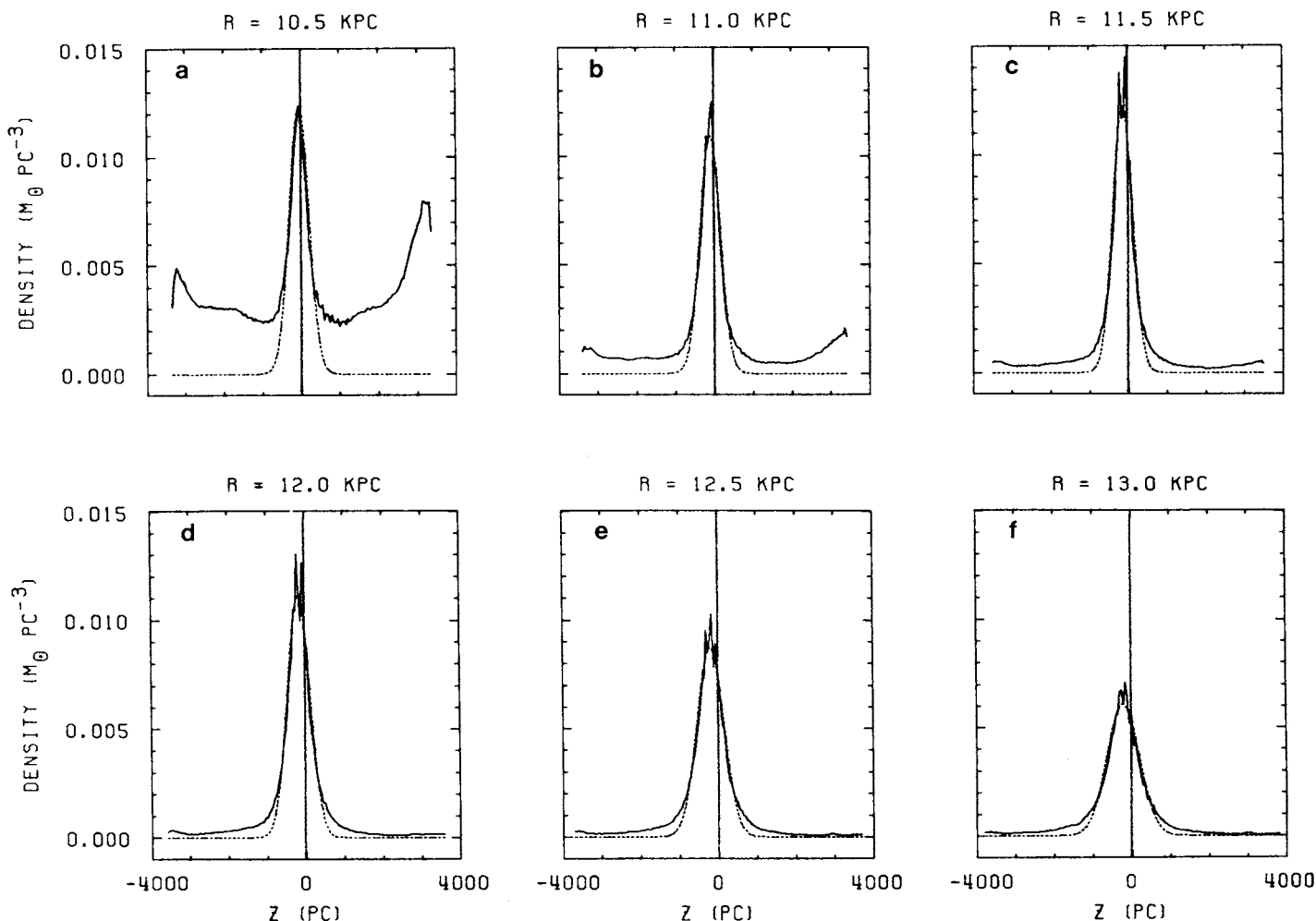
FIG. 16.—Volume density of H I as a function of vertical distance z from the Galactic plane at fixed galactocentric radii beyond the solar circle (analogous to Fig. 9). *Solid line*, data; *dotted line*, best-fit Gaussian. Following HJK, an optical depth correction was applied for calculation of the number density at each l, b, and v: $n_{\mathrm{H\,I}}(l, b, v) = 1.823 \times 10^{18} T_s \tau(l, b, v) | dv/dr |$ atoms cm^{-2} (km s^{-1})$^{-1}$, where r is the (kinematic) distance to the point, T_s ($=125$ K) the (assumed uniform) spin temperature, and $\tau(l, b, v)$ the optical depth; $\tau(l, b, v) = -\ln [1 - T_b(l, b, v)/T_s]$. Each point in z represents an average over 50 pc bins in z and 500 pc rings in R. The label above each plot indicates the galactocentric radius of the center of the ring.

what difficult, so we applied the procedure used to obtain the results for the H_2 to the Parkes H I data. The results are shown in Figure 16 (*solid lines*). It is not clear whether the high-z wings in the H I density profiles are real: the large velocity dispersion of the H I causes some local high-latitude material to appear kinematically at $R > 10$ kpc and ficticiously high z (note especially Fig. 16a), but the wings persist to $R > 13$ kpc; stray radiation entering the antenna's sidelobes also might be partly responsible for the broad wings observed. A simple Gaussian shape in the outer Galaxy is not necessarily expected; for example, in an analysis of H I in the inner Galaxy, Lockman (1984) found the vertical shape of the layer between $R = 4$ and 8 kpc is fitted best by the sum of two Gaussians plus an exponential. On the assumption that in the outer Galaxy the deviation in the shape of the H I layer from a Gaussian is real, the half-thickness and the surface density from the fits (Fig. 16, *dotted lines*) were not used. Instead, the half-width at half-maximum was measured directly from the plots of the data (*solid lines*), and the surface density was taken from the area under the same curves. The symmetry of the curves made possible measurement of the average midplane

directly off the plots as well. Considering the differences between our analysis and that of HJK, the derived quantities generally agree well; in particular, the surface density as a function of galactocentric radius derived here is generally within ~20% of that found by HJK.

Comparisons of the CO and H I z-distribution parameters are shown in Figure 10. (Because of the high velocity dispersion of the H I, the results at $R = 10.5$ kpc were omitted from the comparison.) The H I midplane is within ~25 pc of that of CO out to 12.5 kpc, beyond which very little CO emission is detected. The thickness of the H I layer is about twice that of the CO at all radii. The H I surface density is 5–10 times greater than the H_2 surface density in the outer Galaxy. However, owing presumably to the presence of the Carina arm, we find that the H_2-to-H I surface density ratio in the outer Galaxy has a value in the fourth quadrant that is about twice that in the first and second quadrants reported by SSS from much more limited CO observations. The absence of a counterpart in H I to the peak in the H_2 surface density at 11.5 kpc again indicates the higher velocity dispersion of the H I.

IV. SUMMARY

In this paper we have demonstrated that the kinematics and the spatial distribution of CO justify including molecular clouds in the long-established list of Population I tracers of the Carina arm. The link between molecular clouds and neutral atomic hydrogen in the arm is firm, qualitatively, as indicated by their similar apparent angular and kinematic distributions in the outer Galaxy, and quantitatively, as shown by considering their distributions about the Galactic plane. In a future paper the bridge between H I and stars in the Carina arm will be completed with the cataloging of the Carina arm clouds and the identification of associated star-forming regions. The transformation from the (l, v)-plane to the Galactic plane becomes straightforward once a list of objects, i.e., molecular clouds, is available. We conclude here with a summary of the present results.

1. The Carina arm stands out in the (l, v)-diagram with the characteristic looplike signature of a spiral arm. Its abrupt tangent near $l = 280°$ and zero velocity connects with the near side of the arm at negative velocities within the solar circle and with the far side at positive velocities beyond the solar circle. Extending toward higher longitudes, the near and far sides become separated by as much as 60 km s^{-1}, with only weak (or local) emission between. Although the near side of the arm lies on the locus of terminal velocities, the large clouds identified in this part of the (l, v)-diagram can be placed in the near side of the Carina arm on the basis of their association with well-known optical Carina arm objects.

2. When the emission is integrated over velocity and latitude, a 13-fold jump in intensity is seen as l crosses 280° from below, indicating a comparable arm-interarm contrast in molecular clouds. Owing to velocity integration, streaming motions cannot account for this sharp contrast.

3. The near side, tangent region, and far side of the arm were viewed in the plane of the sky by integrating the emission within the velocity ranges of these kinematically defined features. In the resultant spatial maps, the thinning of the CO layer with increasing kinematic distance, an expected projection effect, supported the kinematic interpretation of the data.

4. Beyond the solar circle, CO and H I are well correlated in both space and velocity, tracing the same large-scale segment of the arm and exhibiting similar concentrations of emission along the arm. Within the solar circle, the CO and H I define similar terminal velocity curves, but the near side of the arm is more difficult to discern as a distinct feature in the H I than in the CO. Similarly, the relative emptiness of the interarm region in the CO (l, v)-diagram has only a weak counterpart in the H I (l, v)-diagram. Although a conspicuous feature in the CO (l, v)-diagram, the Carina arm loop is not as easily discerned in H I.

5. The vertical distributions of the molecular and atomic hydrogen layers in the outer Galaxy were determined and compared. The CO midplane drops progressively downward from the $b = 0°$ plane with increasing distance from the Galactic center, from $z = -48$ pc at $R = 10.5$ kpc to -167 pc at 12.5 kpc. A similar warp was recognized in H I from the earliest 21 cm surveys of the southern Galactic plane, and our analysis of the Parkes data shows the H I midplane to be within ~ 25 pc of the molecular midplane at all radii considered. The half-thickness of the CO layer expands from 112 to 182 pc between 10.5 and 12.5 kpc from the Galactic center, mimicking the long-established flaring of the neutral hydrogen layer, although the scale height of the H I is about twice as great as that of the H$_2$ over the same range of radii. A comparison of the molecular surface densities in the arm and interarm regions yields an arm-interarm contrast of ~ 4.5:1 for the Carina arm, but this ratio is probably a lower limit because (a) the ratio follows from an analysis that tends to wash out nonaxisymmetric (spiral) structure, and (b) a ratio of 13:1 is indicated by the step at $l = 280°$ in the total CO $I(l)$ graph.

APPENDIX

EFFECT OF REVISED GALACTIC CONSTANTS ON THE DERIVED z-DISTRIBUTION

We investigate here how revised values of R_0 and V_0 affect the quantities related to the z-distribution of H$_2$ derived in § IIIa(iv). A flat rotation curve is assumed, and only corrections to first order in ΔR_0 and ΔV_0 are considered. The revised values are taken to be $R_0 = 8.5$ kpc and $V_0 = 220$ km s^{-1} (Kerr and Lynden-Bell 1986), giving $\Delta R_0/R_0 = -0.15$ and $\Delta V_0/V_0 = -0.12$.

With the assumption of a flat rotation curve in the outer Galaxy, $|dv/dr|^{-1}$ takes on a simple analytic form and equation (2) can be expressed as

$$\rho_{l,b,v}(R, z) = \chi T_R(l, b, v)|\sin l|R_0 V_0 R^{-3}(R^2 - R_0^2 \sin^2 l)^{1/2} , \tag{A1}$$

where χ is the numerical constant in equation (2) and $R(l, b, v)$ is galactocentric radius; the "l, b, v" subscript reminds us that this equation represents the density at a single point. For small b, $R(l, b, v) \approx R(l, v)$ and neglecting the $\cos b$ factor in the expression for v, R can be written

$$R(l, v) = V_0[v/(R_0 \sin l) + V_0/R_0]^{-1} . \tag{A2}$$

It follows that the fractional change in the kinematically derived radius of any point is

$$\Delta R/R = \Delta R_0/R_0 + (1 - R/R_0)\Delta V_0/V_0 . \tag{A3}$$

Thus all points (l, v) that map into R have the same change ΔR independent of l and v. In particular, the galactocentric rings in the (l, v)-plane shown in Figure 8 retain their (l, v)-shape with the new values of R_0 and V_0. The radial bins centered at 10.5, 11.0, ..., 13.0 kpc used in our analysis all shift by ~ -1.5 kpc, so the bin spacing, 0.5 kpc, also remains the same.

TABLE 2
FRACTIONAL CHANGES IN z-DISTRIBUTION WITH REVISED R_0 AND V_0

Radius (kpc)	$\Delta R/R$	$\langle \Delta\rho/\rho \rangle$ $(\approx \Delta\rho_0/\rho_0)$	$\Delta z_{1/2}/z_{1/2}$	$\Delta z_0/z_0$	$\Delta\sigma/\sigma$	$\Delta M_T/M_T$
10.5......	−0.14	+0.03	−0.14	−0.14	−0.11	−0.25
11.0......	−0.14	+0.02	−0.14	−0.14	−0.11	−0.25
11.5......	−0.13	+0.01	−0.13	−0.13	−0.12	−0.25
12.0......	−0.13	0.00	−0.13	−0.13	−0.12	−0.25
12.5......	−0.12	−0.01	−0.12	−0.12	−0.13	−0.25
13.0......	−0.11	−0.02	−0.11	−0.11	−0.13	−0.24

From equation (A1), the fractional change in the derived density at any point is

$$\Delta\rho_{l,b,v}/\rho_{l,b,v} = \Delta V_0/V_0 + [1 - \sin^2 l(\alpha^{-2} - \sin^2 l)^{-1}]\Delta R_0/R_0 + [(1 - \alpha^2 \sin^2 l)^{-1} - 3]\Delta R/R , \qquad \text{(A4)}$$

where $\alpha \equiv R_0/R$, and $\Delta R/R$ is given by equation (A3). For $b = z = 0$, $\Delta\rho/\rho$ ranges from 0.06 at $(R, l) = (10.5 \text{ kpc}, 280°)$ to -0.04 at $(13.0 \text{ kpc}, 335°)$. The behavior of $\Delta\rho/\rho$ with R and l can be understood by noting that, with the assumed validity of equation (1), the column density of H_2, $N(H_2)$, may be considered to be a measured quantity. The derived density is just $N(H_2)$ divided by the path length per unit velocity interval, which is function of l, R, and the rotation model. In going from $\rho_{l,b,v}(R, z)$ to the (assumed) axisymmetric $\rho(R, z)$, we have taken weighted averages of $\rho_{l,b,v}$ over l, and it is not necessarily true that the unweighted, numerical average $\langle \Delta\rho_{l,b,v}/\rho_{l,b,v} \rangle_{uw}$ equals the fractional change in the weighted average, $\langle \Delta\rho \rangle_w/\langle \rho \rangle_w$. However, in the case where the *actual* z-distribution *is* axisymmetric, $\langle \Delta\rho_{l,b,v}/\rho_{l,b,v} \rangle_{uw} = \langle \Delta\rho \rangle_w/\langle \rho \rangle_w$ at constant R; we assume this to be the case, and for convenience we drop the "l, b, v" and "uw" subscripts.

The fractional change in the derived central density ρ_0 can now be approximated $\Delta\rho_0/\rho_0 \approx \langle \Delta\rho/\rho \rangle$. At each radius considered in § IIIa(iv), $\langle \Delta\rho/\rho \rangle$ was obtained by computing $\Delta\rho/\rho$ in 1° longitude steps between $l = 280°$ and $335°$. Since $z_0(R)$ and $z_{1/2}(R)$ scale linearly with R, we have for the fractional changes in these quantities $\Delta z_0/z_0 = \Delta z_{1/2}/z_{1/2} = \Delta R/R$. For the fractional change in the surface density σ, we note the good agreement of the fitted and measured results (last two columns in Table 1) and assume $\rho(z)$ is a Gaussian (eq. [3]). Then $\sigma = \int \rho(z)dz = \rho_0 z_{1/2}\sqrt{(\pi/\ln 2)}$, and $\Delta\sigma/\sigma = \Delta\rho_0/\rho_0 + \Delta z_{1/2}/z_{1/2} \approx \langle \Delta\rho/\rho \rangle + \Delta R/R$. Finally, the area A of each galactocentric ring segment scales linearly with R, so $\Delta A/A = \Delta R/R$; the total mass in each ring segment, $M_T = \sigma A$, therefore changes by $\Delta M_T/M_T = \Delta\sigma/\sigma + \Delta R/R$. The computed values of the fractional changes in the derived quantities are given in Table 2. All variations being $\sim 10\%$, our results regarding the z-distribution of H_2 in the outer Galaxy are largely unchanged with the adoption of the revised Galactic constants.

REFERENCES

Allen, C. W. 1973, *Astrophysical Quantities* (London: Athlone).
Bigay, J. H., Garnier, R., Georgelin, Y. P., and Georgelin, Y. M. 1972, *Astr. Ap.*, **18**, 301.
Bloemen, J. B. G. M., *et al.* 1986, *Astr. Ap.*, **154**, 25.
Bok, B. 1937, *The Distribution of Stars in Space* (Chicago: University of Chicago Press).
Bok, B. J., Hine, A. A., and Miller, E. W. 1970, in *IAU Symposium 38, The Spiral Structure of our Galaxy*, ed., W. Becker and G. Contopoulos (Dordrecht: Reidel), p. 246.
Bronfman, L. 1986, Ph.D. thesis, Columbia University.
Bronfman, L., Cohen, R., Alvarez, H., May, J., and Thaddeus, P. 1986, *Ap. J.*, submitted.
Burton, W. B. 1971, *Astr. Ap.*, **10**, 76.
Burton, W. B., and Gordon, M. A. 1978, *Astr. Ap.*, **63**, 7.
Cohen, R. S. 1977, Ph.D. thesis, Columbia University.
Cohen, R. S., Cong, H., Dame, T. M., and Thaddeus, P. 1980. *Ap. J. (Letters)*, **239**, L53.
Cohen, R. S., Dame, T. M., and Thaddeus, P. 1986, *Ap. J. Suppl.*, **60**, 695.
Cohen, R. S., Grabelsky, D. A., May, J., Bronfman, L., Alvarez, H., and Thaddeus, P. 1985, *Ap. J. (Letters)*, **290**, L15.
Dame, T. M. 1983, Ph.D. thesis, Columbia University.
Dame, T. M., Elmegreen, B. G., Cohen, R. S., and Thaddeus, P. 1986, *Ap. J.*, **305**, 892.
de Graauw, T., Lindholm, S., Fitton, B., Beckman, J., Israel, F. P., Nieuwenhuijzen, H., and Vermue, J. 1981, *Astr. Ap.*, **102**, 257.
Georgelin, Y. 1975, Ph.D. thesis, Université de Provence, Observatoire de Marseille.
Gillispie, A. R., Huggins, P. J., Sollner, T. C. L. G., Phillips, T. G., Gardner, F. F., and Knowles, S. H. 1977, *Astr. Ap.*, **60**, 221.
Grabelsky, D. A. 1985, Ph.D. thesis, Columbia University.
Graham, J. A. 1970, *A.J.*, **75**, 703.
Graham, J. A., and Lyngå, G. 1965, *Mem. Mount Stromlo Obs.*, No. 18.
Henderson, A. P., Jackson, P. D., and Kerr, F. J. 1982, *Ap. J.*, **263**, 116 (HJK).

Humphreys, R. M., and Kerr, F. J. 1974, *Ap. J.*, **194**, 301.
Israel, R. P., *et al.* 1984, *Astr. Ap.*, **134**, 396.
Kerr, F. J., and Lynden-Bell, D. 1986, *M.N.R.A.S.*, **221**, 1023.
Kutner, M. L. 1978, *Ap. Letters*, **19**, 81.
Kutner, M. L., Tucker, K. D., Chin, G., and Thaddeus, P. 1977, *Ap. J.*, **215**, 521.
Lebrun, F., *et al.* 1983, *Ap. J.*, **274**, 231.
Liszt, H. S., and Burton, W. B. 1981, *Ap. J.*, **243**, 778.
Lockman, F. J. 1984, *Ap. J.*, **283**, 90.
Loden, L. O., and Sundman, A. 1980, *Astr. Ap.*, **91**, 59.
Mathewson, D. S., Healy, J. R., and Rome, J. M. 1962, *Australian J. Phys.*, **15**, 354.
McCutcheon, W. H., Robinson, B.. J., Whiteoak, J. B., and Manchester, R. N. 1983, in *Kinematics, Dynamics, and Structure of the Milky Way*, ed. W. L. H. Shuter (Dordrecht: Reidel), p. 165.
Mills, B. Y. 1959, in *IAU Symposium 9, Paris Symposium on Radio Astronomy*, ed. R. N. Bracewell (Stanford: Stanford University Press), p. 431.
Neckel, Th., and Klare, G. 1980, *Astr. Ap. Suppl.*, **42**, 251.
Robinson, B. J., Manchester, R. N., Whiteoak, J. B., Sanders, D. B., Scoville, N. Z., Clemens, D. P., McCutcheon, W. H., and Solomon, P. M. 1984, *Ap. J. (Letters)*, **283**, L31.
Rodgers, A. W., Campbell, C. T., Whiteoak, J. B., Baily, H. H., and Hunt, V. O. 1960, *An Atlas of Hα Emission in the Southern Milky Way* (Canberra).
Sanders, D. B., Solomon, P. M., and Scoville, N. Z. 1984, *Ap. J.*, **276**, 182 (SSS).
Sherr, D. 1965, *Quart, J.R.A.S.*, **6**, 299.
Solomon, P. M., Sanders, D. B., and Rivolo, A. R. 1985, *Ap. J. (Letters)*, **292**, L19.
Sundman, A. 1979, *Astr. Ap. Suppl.*, **35**, 327.
Tucker, K. D., Kutner, M. L., and Thaddeus, P. 1973, *Ap. J. (Letters)*, **186**, L13.
White, G. J., and Phillips, J. P. 1983, *M.N.R.A.S.*, **202**, 255.
Wilson, T. L., Mezger, P. G., Gardner, F. F., and Milne, D. K. 1970, *Astr. Ap.*, **6**, 364.

L. BRONFMAN and J. MAY: Departmento de Astronomia, Universidad de Chile, Casilla 36-D, Santiago, Chile

R. S. COHEN: 51 Seventh Ave., Brooklyn, NY   11217

D. A. GRABELSKY: Department of Physics and Astronomy, Northwestern University, Evanston, IL   60201

P. THADDEUS: Harvard-Smithsonian Center for Astrophysics, 60 Garden Street, Cambridge, MA   02138